UNRAVELLING THE HETEROGENEITY OF THE SERPENTINIZED OPHIOLITIC MANTLE (ANTI-ATLAS, MOROCCO): MINERALOGICAL IMPLICATIONS AND LANDSAT OLI-8 MAPPING

Mohamed Ben Massoude*, Amina Wafik*, Hassan Admou*, Daniela Guglietta* and **Rosalda Punturo**,***,✉**

* *Excellence Research Laboratory AQUABIOTECH, GeoSciences Semlalia-Team Geology Department, Fac. Sciences Semlalia, Marrakesh, Morocco.*
** *Institute of Environmental Geology and Geoengineering, National Research Council of Italy (CNR IGAG), Research Area of Rome, Italy.*
*** *Department of Biological, Geological and Environmental Sciences, University of Catania, Italy.*
✉ *Corresponding author e-mail: rosalda.punturo@unict.it*

Keywords: *serpentinite; heterogeneity; lithology; remote sensing; XRPD analyses; Neoproterozoic; Bou Azzer-El Graara Ophiolitic Complex; Morocco.*

ABSTRACT

This study investigates the lithological and mineralogical heterogeneity of the Inguijjem-Aït Ahmane serpentinite massif (Bou Azzer ophiolite, Morocco) using an integrated approach combining field-based petrology and advanced remote sensing. Previously regarded as a homogeneous unit, the massif exhibits significant lithological complexity. Initially, a detailed mineralogical characterization was performed using optical microscopy, X-ray diffraction (XRPD), and micro-Raman spectroscopy to identify and validate the specific serpentinite facies (meta-dunites, meta-harzburgites, meta-wehrlites, and meta-pyroxenites). These ground-truth data were subsequently used to train a supervised classification model based on the Support Vector Machine (SVM) algorithm, applied to Landsat OLI-8 imagery enhanced by Principal Component Analysis (PCA), Minimum Noise Fraction (MNF), and Independent Component Analysis (ICA). The SVM classification successfully discriminated the lithological units, revealing that meta-dunite is the dominant facies, while meta-harzburgites are concentrated in the western sector. The reliability of the mapping was confirmed by a high Overall Accuracy of 97.54 % and a Kappa coefficient of 0.96, demonstrating the robustness of the model. The study highlights that despite intense serpentinization, the observed spectral heterogeneity reflects primary lithological variations rather than secondary alteration patterns. These findings underscore the effectiveness of coupling detailed mineralogical analysis with machine-learning techniques for mapping complex ophiolitic terrains.

INTRODUCTION

The Bou Azzer-El Graara inlier, located in the Anti-Atlas region of Morocco, is a geologically significant site due to its complex tectonic history and lithological geodiversity. Indeed, this area exposes well-preserved sections of oceanic crust and upper mantle, providing an exceptional window into the geodynamic and petrological processes associated with subduction zones and island arc environments.

The formation of Bou Azzer-El Graara is closely linked to the tectonic history of the West African Craton (WAC) and the Pan-African orogeny. During the Archean, the WAC underwent a series of tectonic collisions and subductions that shaped its current structure (Ennih and Liégeois, 2008). During the Pan-African orogenic phase, the convergence of tectonic plates led to the subduction of oceanic crust beneath various oceanic arcs (Black et al., 1979, 1994; Hefferan et al., 2000; Ennih and Liégeois, 2001; Hefferan et al., 2014), creating conditions favorable for partial melting, metasomatism, and serpentinization of mantle peridotites (Wafik et al., 2001a; 2001b; 2015). These processes led to the formation of a complex ophiolitic assemblage comprising ultramafic rocks, gabbros, volcanic rocks, and volcanosedimentary rocks.

The ultramafic rocks of Bou Azzer, representing the basal unit of this assemblage, are particularly remarkable (Leblanc, 1975; Bodinier et al., 1984). They constitute a 4 to 5-kilometer-thick section, separated by tectonic discontinuities and intruded by syn- to post-kinematic plutons (Saquaque et al. 1989). These geological units, well described by Leblanc (1981), Bodinier et al. (1984), Saquaque et al. (1989), and earlier foundational research, provide critical insights into the formation conditions and dynamic geological processes of that era.

Most authors describe the serpentinized massif of Ait Ahmane as a single green facies. However, this simplified representation may obscure its significant geological complexity.

Remote sensing has long been recognized as an effective tool for geological cartography, particularly for the detection and mapping of ophiolitic complexes and associated lithologies. Numerous studies conducted in regions such as Egypt, Pakistan, and Iran have demonstrated the capability of multispectral and hyperspectral satellite data to discriminate among mafic–ultramafic units, serpentinized peridotites, metamorphic assemblages, and tectonic mélanges due to their diagnostic spectral absorption features in the visible, near-infrared, and shortwave infrared domains (Amer et al., 2010 ; Khaneghah and Arfania 2017; Khurram et al., 2025). Landsat, ASTER, Sentinel-2, and Hyperion datasets have been widely applied to characterize chromite-rich peridotites, altered harzburgites, gabbros, and metavolcanic sequences, enabling lithological classification, structural analysis, and mineralogical mapping in complex ophiolitic terrains (Bentahar and Raji, 2021). These previous applications provide a robust scientific framework that supports the relevance of remote sensing techniques in similar geological settings and justify the use of Landsat-8 OLI data for the lithological discrimination carried out in this study.

Although the Bou Azzer-El Graara inlier is a key area for understanding Pan-African suture zones, the internal lithological architecture of the serpentinized massifs remains poorly constrained. A major scientific challenge lies in the difficulty of discriminating between varying ultramafic protoliths (e.g., dunite vs. harzburgite and wehrlite) that have been obscured by intense serpentinization and surface alteration. Consequently, existing geological maps often ascribe the various lithotypes to the generic 'serpentinite' units, masking the true mantle heterogeneity.

Therefore, this study addresses a twofold purpose: (1) To overcome the spectral similarity of these facies by integrating advanced machine learning (SVM) with rigorous field mineralogy (Raman/XRPD); and (2) To produce a high-resolution lithological map that reveals the internal structure of the Inguijjem-Aït Ahmane massif. Unraveling this heterogeneity is crucial not only for targeting Co-Ni-mineralization but also for reconstructing the geodynamic evolution of the ophiolitic sequence.

STUDY AREA

The Bou Azzer-El Graara inlier is located in the southeastern part of the central Anti-Atlas, on the northern edge of the WAC (Fig. 1a). This inlier, oriented WNW-ESE, corresponds to a Variscan antiform megastructure. It extends approximately 65 km along both sides of the major Anti-Atlas fault (AAMF) (Fig. 1b). The ophiolitic rocks of this inlier cover an area of 15 km long and 4 km wide. They are composed of serpentinized peridotites, intersected by a network of basic and ultrabasic dykes, cumulates, gabbros, microgabbros, spilite basalts, and diabases, as well as a volcano-sedimentary complex (Leblanc 1975, 1981). The presence of one of the world's eldest ophiolites, namely the Pan-African suture zone marked by the AAMF, as well as its significant metallogenic richness, have made this region a key site for understanding the geological history. It has been the subject of numerous studies and debates focusing on both lithostratigraphic and geodynamic aspects (Leblanc, 1975; Saquaque et al., 1989; Hefferan et al., 2000; Thomas et al., 2002; El Hadi et al., 2010).

The Bou Azzer ophiolitic sequence, located at the core of the Bou Azzer-El Graara anticline, is mainly composed of serpentinized harzburgites and dunites, representing in volume about 70% of the sequence (Leblanc, 1975, 1981). This sequence is bordered by bands of ultramafic and mafic metacumulates, including pyroxenites, chromite pods, and foliated and isotropic metagabbros, as well as remnants of basalts forming the dyke complex and pillow lavas. The geo-

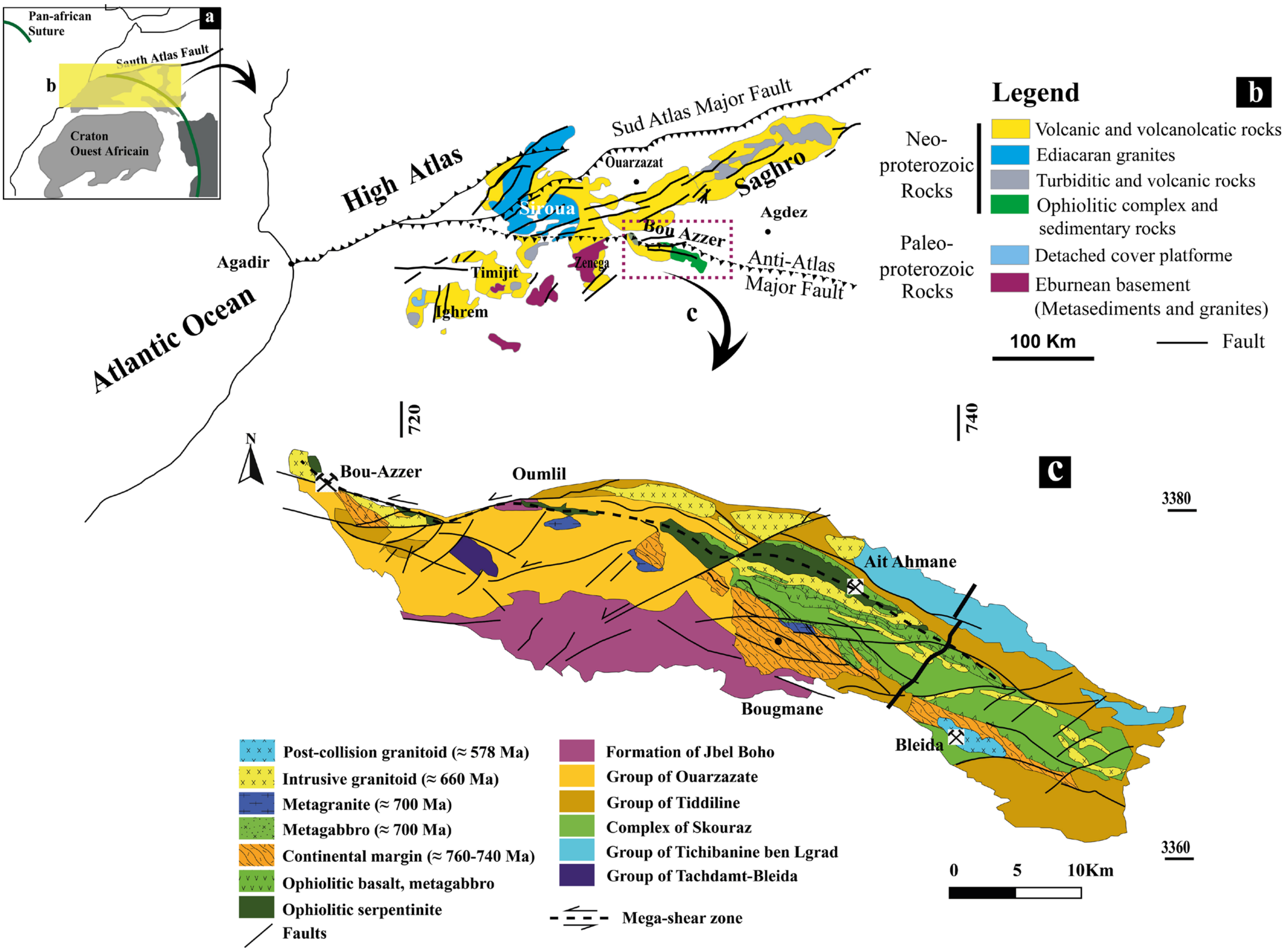

Fig. 1 - a) Location of the Anti-Atlas range at the boundary of the West African craton (WAC); b) Simplified geological map of the Anti-Atlas showing the location of the study area (modified after Gasquet et al., 2008, and Soulaimani et al., 2018); c) Simplified geological map of the Bou-Azzer El Graara inlier (modified after Leblanc, 1981, and Wafik et al., 2025a).

chemical signatures of the basalts indicate an affinity with a supra-subduction zone, suggesting formation in a back-arc or fore-arc extension basin (Bodinier et al., 1984; Naidoo et al., 1991).

The Bou Azzer serpentinites form a main massif that extends from Ait Ahmane to Ambed (Fig. 1c). This massif is offset by the NE-SW trending dextral Irhtem fault, illustrating the significant impact of regional tectonic movements. Besides this main massif, serpentinites also appear as small lenticular bodies scattered within the inlier, such as at Bou Azzer, Aghbar, Oumlil, Bouismas, and Tamdrost. These serpentine bodies extend along a northwest-southeast trend (Wafik et al., 2024).

The serpentinites of the ophiolitic complex exhibit a variety of facies ranging from light to dark green, reflecting variations in their mineral composition and distinct boundaries between different zones (Wafik et al., 2015). The presence of magnetite, chromian spinels, and sulfides, along with their association with talc-carbonates, indicates the transformation of serpentinized ultramafic rocks into silica-carbonate-rich rocks, a phenomenon that occurs primarily along faults and shear zones (Wafik et al., 2015). Serpentinization temperatures are estimated between 200°C and 350°C (Klein et al., 2013; Bonnemains et al., 2016). The intrusions of dioritic to granodioritic plutons, containing mafic enclaves, indicate magmatic activity in an intra-oceanic context, with emplacement ages around 640 to 660 Ma (Inglis et al., 2005; El Hadi et al., 2010; Walsh et al., 2012; Blein et al., 2014).

METHODOLOGY

To study the serpentinized massifs of the Bou Azzer-El Graara ophiolitic complex, a multidisciplinary approach was adopted, combining satellite imagery, mineralogical analysis, and field validation. This methodology integrates large-scale observations with detailed in situ and laboratory analyses.

Field data

During the initial field observation, a striking chromatic diversity of the serpentinite lithotypes was immediately noticeable. At the mesoscale, the hues vary from beige to light green, then to dark yellow-green and blackish (Fig. 2); such variations are also recognizable at the scale of the outcrop (Fig. 5a).

In order to analyze the different facies of the serpentinized massifs, three one-week field missions were conducted in the Bou Azzer ophiolitic complex. A total of 124 samples were collected from various serpentinite bands, covering a wide range of mineralogical compositions and tectonic contexts. Each sample was carefully geolocated and documented to ensure maximum representativeness of the geological variations in the study area (Fig. 3).

These samples underwent a hierarchical screening process, starting with an initial macroscopic grouping based on field criteria (i.e. microstructure, color, alteration) followed by petrographic validation using optical microscopy. From this screened dataset, 11 representative type-specimens covering all of the identified classes were selected for quantitative X-ray powder diffraction (XRPD) and micro-Raman analysis. This targeted selection aimed to avoid analytical redundancy while ensuring a complete characterization of each facies. Finally, crustal units such as quartz-diorites and associated clastic sediments were excluded from the micro-analytical dataset to align with the study's primary objective of specifically discriminating among serpentinite facies, thereby focusing the analytical effort exclusively on the mantle sequence.

Mineralogical and Petrographic Investigation

A detailed study of 11 representative type specimens was conducted to characterize the mineralogical composition and to identify the microstructural features and relationships.

Thin sections were prepared from the selected rock samples and analyzed using a Leica DM750 P polarizing microscope. Observations were carried out under plane-polarized (PPL) and cross-polarized (XPL) light using various objectives (4× to 40×) to identify primary relict phases and serpentinization microstructures.

For quantitative mineralogy, the samples were ground into a fine powder (<20 μm) using a mortar grinder. To counteract the preferred orientation of sheet silicates (serpentine minerals), the powders were mounted using the back-loading technique. This approach promotes random particle orientation,

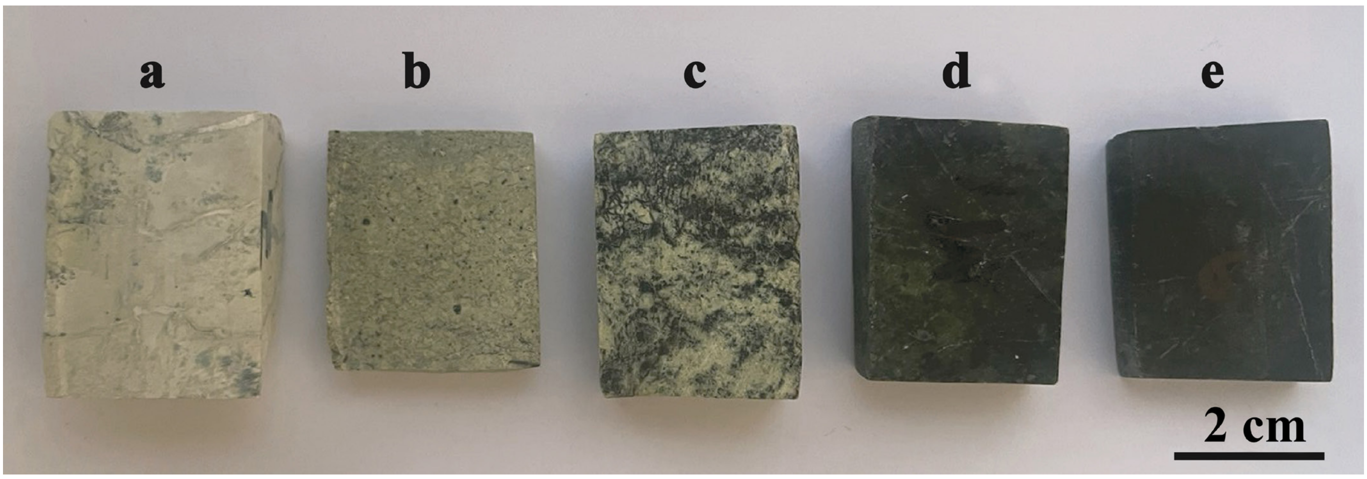

Fig. 2 - Different serpentinite samples were collected in the study area during in- situ campaign. Based on the color: a) beige to gray serpentinite, b) green serpentinite, c) green yellow serpentinite, d) dark green serpentinite, e) dark serpentinite.

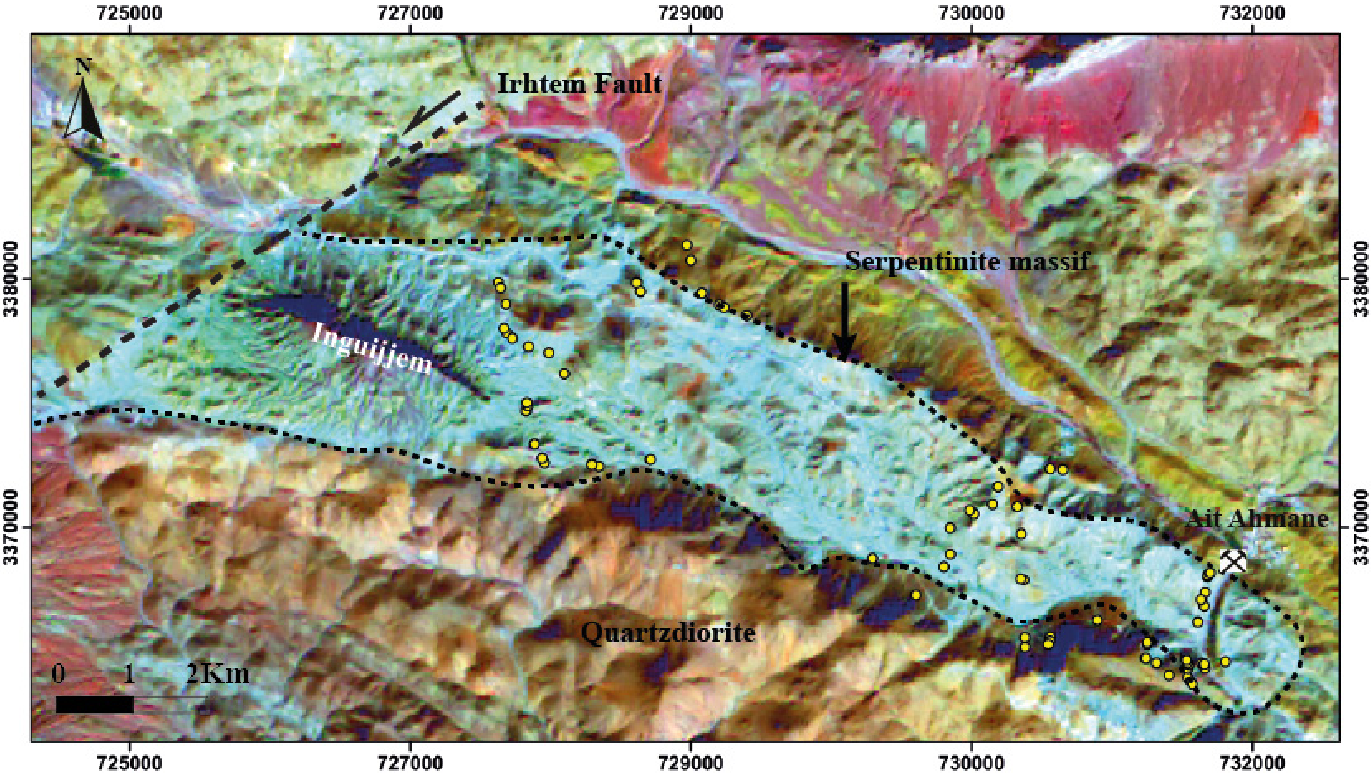

Fig. 3 - Samples collected in the Serpentinite Massif of the Bou Azzer-El Graara Ophiolite are overlaid on Pan Sharpening Landsat 8 OLI Imager (R: Band 1, G: Band 2, B: Band 3), WGS 1984 UTM Zone 29N.

ensuring reliable relative intensities in the diffraction patterns. Diffraction data were acquired using a Rigaku Smart Lab SE XRPD diffractometer, employing monochromatic Cu Kα1 radiation (λ = 1.5406 Å) at 40 kV and 30 mA. The instrument was equipped with an X'Celerator detector. Patterns were recorded in the 2θ range of 5° to 90°.

Semi-quantitative phase analysis was performed via the Rietveld refinement method using HighScore Plus software. The structural models used for the refinement were based on crystallographic information files (.cif) sourced from the Crystallography Open Database (COD). Weight fractions obtained from Rietveld refinement were converted to volume percentages using mineral densities, in order to allow direct comparison with petrographic modal mineralogy (Delesse principle; e.g., Tzvetanova et al., 2020). The statistical quality of the refinements was monitored using standard reliability factors. While these statistical indicators represent acceptable mathematical fits for highly disordered phyllosilicate-rich assemblages, the resulting phase proportions are considered semi-quantitative due to the inherent crystallographic complexities of serpentinites. To unequivocally distinguish among the serpentine polymorphs (lizardite, antigorite, and chrysotile) and characterize the mineral phases observed via optical microscopy, in-situ Micro-Raman spectroscopy analyses were conducted on polished thin sections. Raman spectra were acquired at the Centre of Analysis and Characterization (CAC) of Cadi Ayyad University (Marrakech, Morocco), using a confocal Horiba Jobin Yvon LabRAM HR Evolution spectrometer. Excitation was provided by a solid-state laser source with a wavelength of 532 nm, focused onto the sample surface through an Olympus ×50 objective lens. The spectral range was configured to cover both the lattice vibration region (100-1200 cm^{-1}) and the diagnostic OH-stretching region (3600-3800 cm^{-1}), which is critical for discriminating between serpentine varieties. Spectrometer calibration was verified daily using the characteristic silicon band at 520.7 cm^{-1}. Data acquisition and processing (including baseline correction and smoothing) were performed using LabSpec 6 software.

Consequently, the differentiation of the ultrabasic lithotypes was achieved through a combined approach: evaluating the relative modal proportions of serpentine polymorphs and relict phases from XRD and Raman spectra, systematic cross-validation with bulk-rock geochemical normative calculations, and the analysis of characteristic pseudomorphic microstructures.

Satellite imagery and Satellite Data Preprocessing

This study is based on the analysis of the Landsat 8 OLI (Operational Land Imager) satellite image acquired on December 20, 2023, and downloaded from the United States Geological Survey (USGS) website (https://earthexplorer.usgs.gov/). The main characteristics of the Landsat 8 OLI image are summarized in Table 1. Spectral bands (1 to 7) contain critical information for characterizing the mineralogical composition of rocks. Furthermore, the thermal infrared bands of Landsat 8 have significantly improved the accuracy of remote sensing in this spectral range, thereby facilitating lithological mapping. The image was georeferenced using the UTM projection system (zone 29) and dated according to the WGS84 model. The reported geometric accuracy, based on ground control points, indicates a root mean square error (RMSE) of 5.75 meters, ensuring high quality for lithological analysis.

The processing of the Landsat 8 OLI image began with a series of preprocessing steps to ensure data quality and reliability. Atmospheric correction was performed to reduce the effects of atmospheric particles and gases, enhancing the spectral quality of the data. Radiometric correction was applied to adjust pixel values and account for variations caused by imaging conditions, ensuring consistent radiometric measurements. Spatial enhancement techniques were employed to improve image resolution and clarify geographic details, as illustrated in Figure 4. These preprocessing steps were conducted using tools in ENVI (Environment for Visualizing Images) software, version 5.6, to guarantee accurate and high-quality data preparation for subsequent analysis.

Image processing

After pre-processing, the images undergo a series of processing analyses (Fig. 4). The PCA reduces the dimensionality of the data, facilitating the interpretation and classification of geological features (Amer et al., 2012). MNF enhances image quality by separating the signal from noise, allowing for better distinction of geological formations (Zhang et al., 2016; Ge et al., 2018). The MNF method reduces noise and extracts key information from hyperspectral or multispectral data (Marzouki and Dridri 2023). It transforms the data into a new space where components are ranked according to their signal-to-noise ratio. The initial components contain most of the useful information, while the later components are primarily noise. ICA decomposes the data into independent components to identify specific spectral signatures of different lithologies (Adiri et al., 2020). The collected field data are then integrated to validate and refine the geological interpretation, leading to the production of a detailed and accurate lithological map. The images were processed using ENVI (Environment for Visualizing Images) software version 5.6.

Support Vector Machine Classification (SVM)

Support Vector Machine (SVM) classification, originally proposed by Vapnik (1999), is based on finding an optimal hyperplane that separates classes in an n-dimensional feature space. This method uses a training dataset to define the decision boundary that maximizes the margin between data points from different classes. The data points closest to this boundary, known as support vectors, play a critical role in determining the hyperplane. To handle non-linear distributions, data can be transformed into a higher-dimensional space using kernel functions. For pixel classification, the algorithm evaluates the position of each feature vector relative to the hyperplane, assigning each pixel to the class corresponding to the side of the hyperplane on which it lies.

The classification was implemented using the ArcGIS Pro 3.0 software. Following the recommendations of Yang (2011), for remote sensing applications, we selected the Radial Basis Function (RBF) kernel, as it yields the best performance for non-linearly separable geological classes. The model was fine-tuned with a penalty parameter set to 100, a value specifically chosen to minimize misclassification in spectrally similar lithologies, and a gamma value calculated as the inverse of the number of input bands.

Unlike standard spectral classifications, the input feature space for this study was constructed by stacking the Landsat OLI-8 spectral bands with the decorrelated components derived from PCA, MNF, and ICA. These transformed features were selected for their high information content and low inter-band correlation.

Table 1 - Characteristics of the Landsat 8 OLI image

Bands	Common Name	Wavelength (µm)	Resolution (m)
Band 1	Coastal aerosol	0.43 -0.45	30
Band 2	Blue	0.45 - 0.51	30
Band 3	Green	0.53 -0.59	30
Band 4	Red	0.64 -0.67	30
Band 5	Near Infrared (NIR)	0.85 -0.88	30
Band 6	SWIR 1	1.57 -1.65	30
Band 7	SWIR 2	2.11 -2.29	30
Band 8	Panchromatic	0.50 -0.68	15
Band 9	Cirrus	1.36 -1.38	30
Band 10	Thermal Infrared (TIRS) 1	10.60 – 11.19	100 * (30)
Band 11	Thermal Infrared (TIRS) 2	11.50 – 12.51	100 (30)

Table 2 - Definition of regions of interest (ROIs) used as input in the SVM algorithm

	Landsat OLI-8 image		
ROIs	**Pixel. No**	**Field sample**	**Coverage Area (m^2)**
Meta-D-W	12	BMAA35; ST1; ST2; BA11; JO9 ; SA	2,700
Meta-H	35	BMAA14 ; BMAA5b ; BMAA52	7,875
Px-Gb	46	BMI2 ; I3	10,350
Q-D	15	-	3,375
Cls	14	-	3,150

Meta-D-W: Meta-dunite-Wehrlite, Meta-H: Meta-Harzburgite, Px-Gb: Pyroxenite–Gabbro, Q-D: Quartz Diorite and Cls: Clastic Sediments.

Finally, to produce a homogeneous lithological map and reduce «salt-and-pepper» noise, a sieve filter was applied to the classified output using PCI Geomatica software. This post-processing step merged isolated pixel groups smaller than 100 pixels with their largest neighboring class.

Regions of Interest (ROIs) were defined based on the precise coordinates of the field samples to ensure a direct link between the spectral signatures and the mineralogical composition. Specifically, the samples characterized by XRPD and petrography (listed in Table 2 and detailed in Table 1S) served as the primary ground truth for training the SVM model. These point-data were supplemented by visual interpretation of high-resolution GeoEye imagery (Google Earth) and geological maps to define representative training polygons. This methodology ensures that the remote sensing classification is strictly constrained by the quantitative mineralogical data obtained in the laboratory.

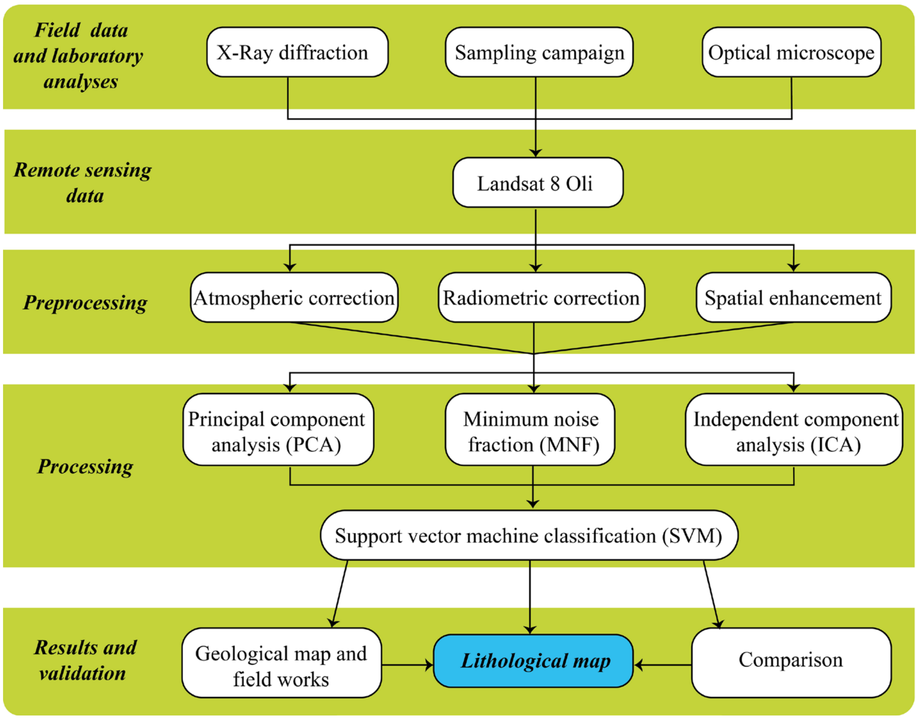

Fig. 4 - Flowchart of the Main Steps for Pre-Processing and Processing Landsat 8 OLI Image.

Accuracy Assessment

The evaluation of classification performance was conducted using validation data derived from reliable reference points. Various indicators were employed to analyze this performance, including the kappa coefficient (k_c), overall accuracy (OA), producer's accuracy (PA), and user's accuracy (UA) (Congalton and Green, 2019). The kappa coefficient is a statistical index that measures the agreement between classification results and reference values. A kappa value close to 1 indicates strong agreement, whereas a value near 0 reflects weak correspondence. Overall accuracy corresponds to the total percentage of pixels correctly classified relative to the total number of pixels in the evaluated image, thus providing a global measure of classification quality. User's accuracy represents the proportion of pixels assigned to a given class that actually belong to that class, highlighting commission errors. By contrast, producer's accuracy denotes the proportion of pixels in a specific class that were correctly identified, allowing for the quantification of omission errors.

The k_c, OA, PA, and UA were calculated using:

$$K_c = \frac{(N\sum_{i=1}^{r} n_{ii}) - (\sum_{i=1}^{r} n_{icol} \cdot \sum_{i=1}^{r} n_{\mathrm{irow}})}{N^2 - (\sum_{i=1}^{r} n_{\mathrm{icol}} \cdot \sum_{i=1}^{r} n_{irow})}$$

$$OA = \frac{\sum_{i=1}^{r} n_{ii}}{N}$$

$$PA = \frac{n_{ii}}{n_{icol}}$$

$$UA = \frac{n_{ii}}{n_{irow}}$$

In this context, n_{ii} represents the number of pixels accurately classified within a specific category. N denotes the total number of pixels in the confusion matrix, while r corresponds to the total number of rows. Additionally, n_{icol} and n_{irow} refer to the total number of pixels in the column (representing reference data) and the row (representing predicted classes), respectively.

These metrics provide a detailed assessment of the reliability and accuracy of the classification model, enabling the identification of its strengths and weaknesses in distinguishing between classes.

RESULTS

Lithological Facies and Macroscopic Observations

Each variety of serpentinite appears as bands or lenticular bodies, juxtaposed with one another (Fig. 5a and c). This configuration sometimes makes it difficult to distinguish between the different varieties, as they are often interpenetrated without clear boundaries. The gradual transition between colors and textures underscores the heterogeneity and mineralogical complexity of the massif.

The serpentinites of the Inguijjem-Ait Ahmane massif exhibit a varied range of colors, with each hue revealing information about their composition and degree of alteration. Beige to yellow-green serpentinite (Fig. 2a and Fig. 5a, b) is often talcified, indicating that the serpentine has been partially or completely transformed into talc. The light green to dark yellow-green varieties (Fig. 2b and c) may signal less altered serpentinite or a distinct mineralogical composition, with a higher proportion of chrysotile, which tends to have a paler hue. The serpentinites ranging from dark yellow-green to blackish (Fig. 2d, e, and Fig. 5b) represent the most common color, generally due to the presence of serpentine minerals such as antigorite and lizardite. These dark hues indicate low hydrothermal alteration and a composition rich in iron and magnesium. The pyroxenite associated with the Bou Azzer ophiolite occurs as dark, fine- to medium-grained, massive lenses and layers intercalated within the ultramafic units (Fig. 5d). They typically display a compact structure and a mineral assemblage dominated by pyroxene.

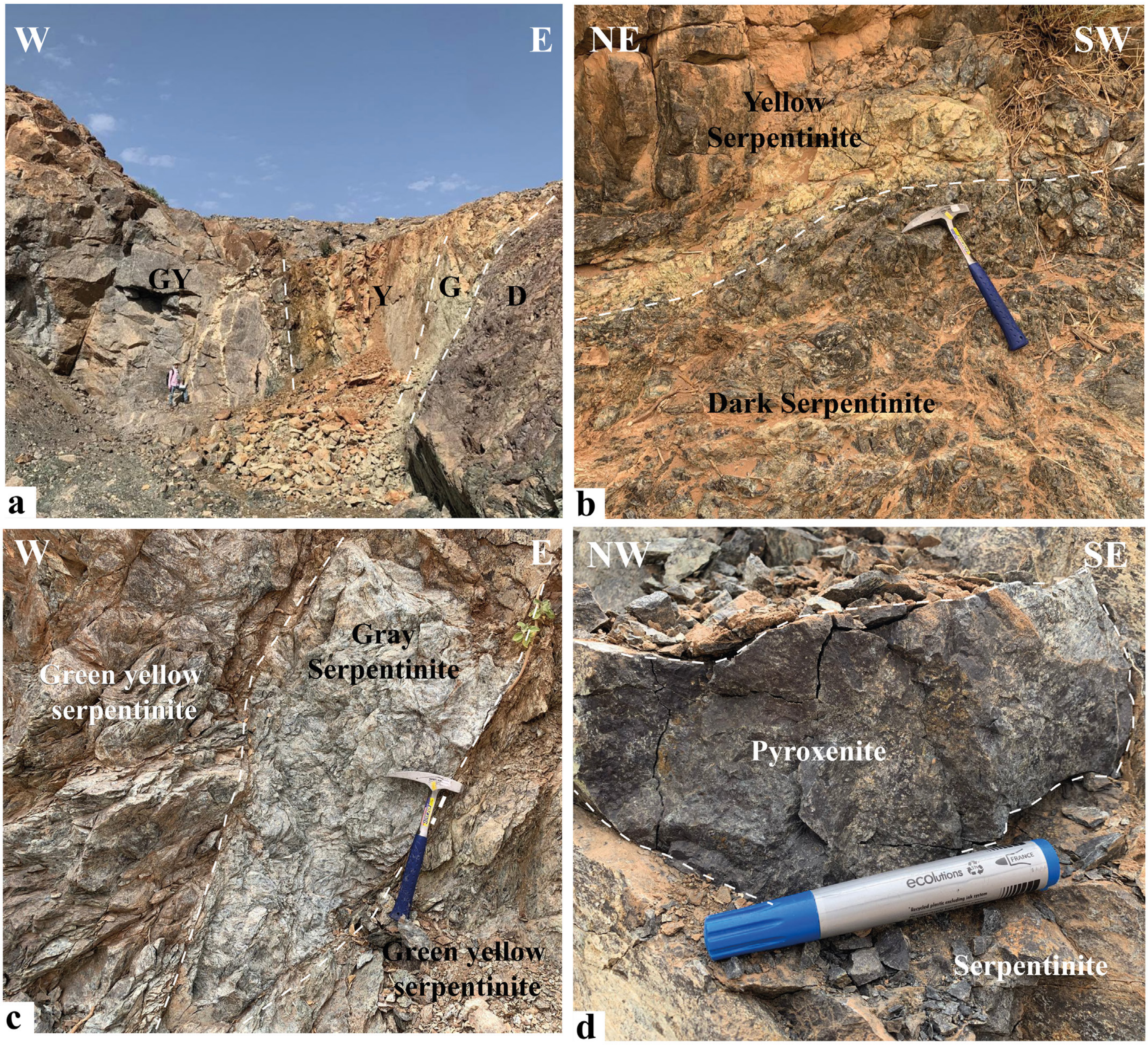

Fig. 5 - Detailed outcrop features: a) Serpentinite bands (GY: green-yellow serpentinite, Y: yellow serpentinite, G: green serpentinite, D: dark serpentinite); b) The boundary between two varieties of serpentinite (yellow and dark, respectively); c) One band of grayish serpentinite intercalated between two bands of yellow-green serpentinite; d) Pyroxenite within serpentinite.

Mineralogical and microstructural characterization

Microscope examination of thin sections confirms the lithological differentiation observed in the field and highlights specific microstructural variations as well as mineral assemblages for each facies.

The dunite samples, represented by specimen BMAA35, are dominated by a pseudomorphic mesh texture (Fig. 6a), reflecting the pervasive serpentinization of the original olivine cumulates. The mesh rims are composed of fibrous lizardite and antigorite, while the mesh cores appear isotropic or cryptocrystalline. Secondary talc patches that overprint the primary serpentine mesh (Fig. 6a), indicating a subsequent stage of metasomatic crystallization.

In contrast to the ordered mesh of dunite, the wehrlite, represented by specimen SA, exhibits a heterogeneous, interpenetrating microstructure (Fig. 6b). The matrix is largely composed of interlocking antigorite blades and of irregular patches of talc, suggesting a higher degree of recrystallization or deformation. The primary texture is almost entirely obliterated, and the rock is frequently crosscut by late-stage veinlets filled by cross-fiber chrysotile.

The meta-harzburgite (e.g., specimen BMAA5b) is unequivocally distinguished by the presence of large bastite pseudomorphs. These tabular microstructures replace the primary orthopyroxene crystals while preserving the original cleavage planes and crystal habit. The bastite aggregates are composed of fibrous lizardite oriented along the original crystallographic elements; moreover, bastite aggregates are embedded within a fine-grained serpentine matrix (Fig. 6c).

The pyroxenite facies (e.g., specimen BMI2) displays the lowest degree of serpentinization among the studied units. It is characterized by a granular microstructure with well-preserved primary magmatic minerals. Under the microscope, large, fractured crystals of clinopyroxene and orthopyroxene are clearly visible, exhibiting high birefringence colors. Secondary recrystallization is restricted to grain boundaries and intragranular fractures, which are filled with minor amounts of serpentine and iron oxides, leaving the core of the pyroxenes intact.

Quantitative Mineralogy and Phase Identification

The X-ray diffraction patterns reveal a mineralogical evolution closely linked to the degree of serpentinization and the initial protolith composition. Representative XRD patterns for the four main lithotypes are shown in Figure 7. However, accurate identification and quantification of these materials using XRD alone are inherently limited. In the specific case of serpentinites, Rietveld Analysis alone is insufficient to guarantee absolute quantification, given the major challenges associated with phyllosilicates: severe diffraction peak overlapping, the lack of an internal standard, and high structural disorder. Consequently, the results derived from this processing (Table 1S) can only be considered semi-quantitative, providing only relative percentages of the crystalline phases. Because these mineralogical estimations form the foundation for our subsequent interpretations (particularly for remote sensing), overcoming these analytical limitations was essential. It is precisely for this reason that the relative XRD data were systematically complemented, supported, and cross-validated by bulk-rock geochemical characterization and normative calculations (see Table 3 in Wafik et al., 2026, in press). Only this combined approach ensures the robustness and reliability of the quantitative mineralogy presented herein.

In the serpentinized peridotites (i.e. dunite, wehrlite and harzburgite), it is worth noting that the primary assemblage is largely replaced by serpentine polymorphs dominated by antigorite, which constitutes the main component of the rock matrix in massive meta-harzburgites (up to 63.2 vol.%) (Fig. 6c and 7c), meta-wehrlites (~59 vol%) (Fig. 6b and 7b) and typical meta-dunites (Fig. 6a and 7a). Lizardite occurs as a subordinate mineral phase (typically 5–15 vol.%), often associated with either mesh textures and bastites, whereas the abundance of chrysotile is highly variable. Ranging from ~16 vol.% in massive samples to nearly 50 vol.% in the intensely

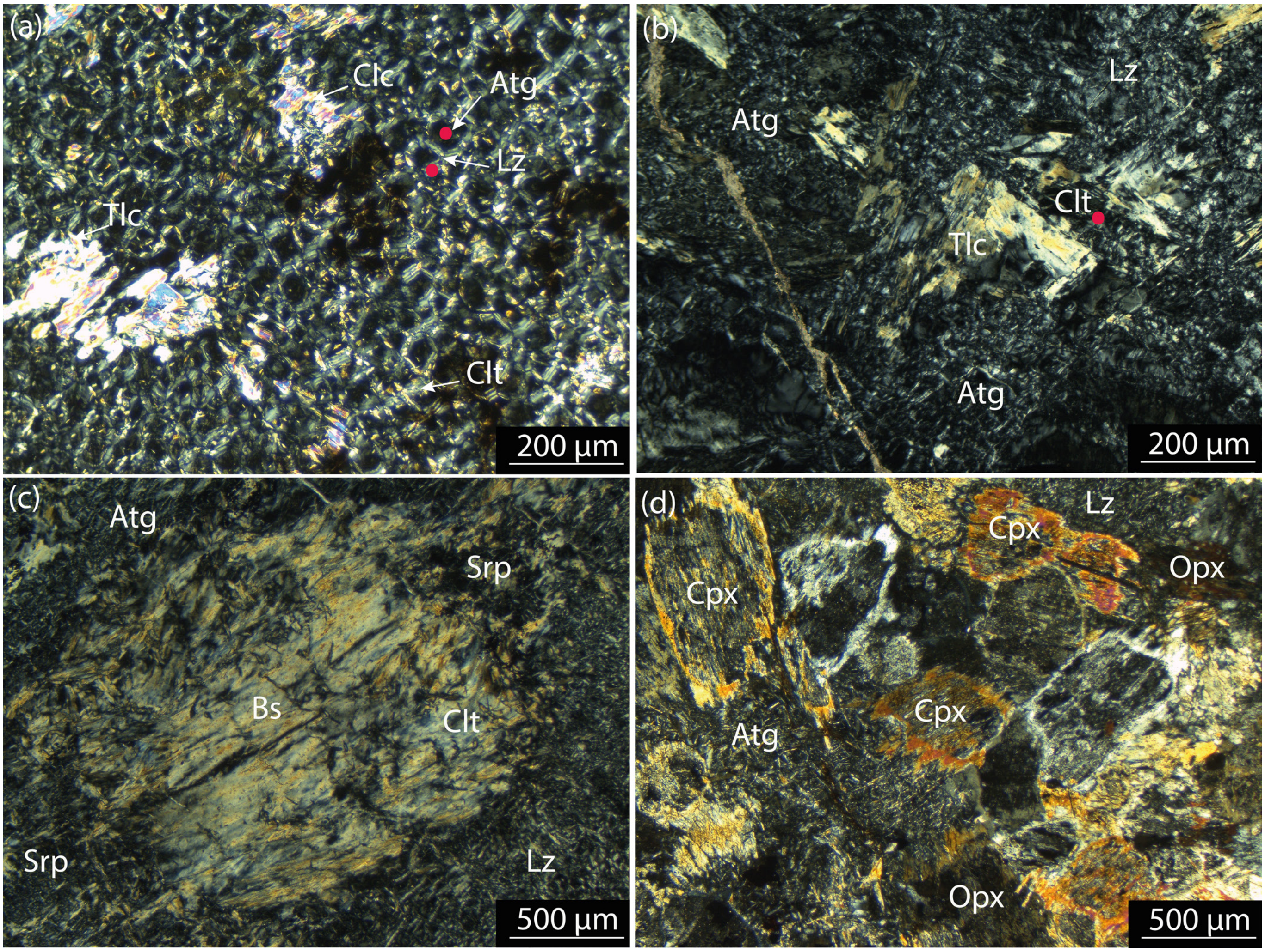

Fig. 6 - Photomicrographs of the studied ultramafic facies. Red dots indicate micro-Raman analysis spots. (a) Meta-dunite: Displays a typical pseudomorphic mesh texture with lizardite (Lz) rims and isotropic cores; secondary talc (Tlc) patches are observed. (b) Meta-wehrlite: Exhibits a complex texture dominated by antigorite (Atg) and talc (Tlc) with late-stage chrysotile (Clt) veins, reflecting the alteration of an olivine-clinopyroxene assemblage. (c) Meta-harzburgite: Characterized by large bastite (Bs) pseudomorphs after orthopyroxene embedded in a serpentinized matrix; Srp: Serpentinite (d) Meta-pyroxenite: Shows a granular texture with preserved primary magmatic minerals, including large crystals of clinopyroxene (Cpx) and orthopyroxene (Opx) surrounded by minor alteration products.

Table 3 - Bulk-rock geochemical composition and normative calculations of the main lithotypes in the study area (Wafik et al. 2026 in press)

Sample	Rock	Plagioclase (Anorthite)	Diopside	Hypersthene	Olivine	Larnite	Ilmenite	Magnetite	Chromite	Total
BMAA35	Dunite	1.8	-	-	94.55	0.06	0.02	2.99	0.55	100
SA	Wehrlite	1.07	12.06	-	83.11	0.22	0.02	2.78	0.45	100
BMAA 5b	Harzburgite	1.57	-	42.08	53.27	-	0.02	2.17	0.3	100
BM I 2	Orthopyroxenite	1.51	-	79.26	15.84	-	0.02	2.46	0.29	100

fractured meta-dunites, the high chrysotile content correlates directly with the macroscopic fibrous vein networks, observed at the scale of the outcrop.

A distinctive feature observed in the meta-peridotite samples is the presence of talc, as also displayed by the XRD patterns (Figure 7a-c); moreover, Rietveld quantification indicates talc content reaching 21.6 vol% in meta-dunite (specimen BMAA35), confirming a significant steatitization event that overprints the initial serpentinization. Additionally, clinochlore is frequently detected (up to ~16 vol.%), particularly in specimens where alumina was available (e.g., altered pyroxene-bearing facies), consistent with the breakdown of aluminous phases. Minor amounts of magnetite and brucite have also been quantified, reflecting the iron and magnesium release during the serpentinization process.

The meta-pyroxenite (Fig. 6d and 7d) is the least transformed lithotype. Its diffractogram highlights the occurrence of clinopyroxene (i.e. diopside) and of orthopyroxene (i.e. hypersthene). Quantitative analysis confirms this preservation, with diopside reaching up to 59.3 vol% and hypersthene up to 79.4 vol% (Table 1S). In these samples, serpentine minerals represented by lizardite and antigorite are minor (<15 vol.%) and likely restricted to grain boundaries and fractures.

Finally, complementary to X-ray diffraction, Raman spectroscopy was employed to accurately discriminate among serpentine polymorphs within the investigated meta-ultramafic rocks. Figure 8 displays the characteristic obtained Raman spectra. Identification relies primarily on the hydroxyl group stretching vibration region (3600-3800 Cm^{-1}), which serves as a diagnostic fingerprint for each polymorph.

Antigorite is distinguished by a sharp, characteristic peak at 3668 cm^{-1}, accompanied by a secondary peak near 3697 cm^{-1}. Lizardite exhibits a relatively complex profile in this region, with main bands located at 3684 cm^{-1}, 3696 cm^{-1}, and 3704 cm^{1}. Finally, chrysotile, where present, is dominated by an intense, asymmetric peak centred at 3698 cm^{-1}.

In the low-frequency region (< 1200 cm^{-1}), crystal lattice vibration modes (Si-O) further corroborate these identifications, notably with peaks observed near 230 cm^{-1} and 690 cm^{-1} for antigorite. This analysis confirms the coexistence of these mineral phases within the studied meta-serpentinite assemblages.

Principal Component Analysis (PCA)

Principal Component Analysis (PCA) applied to the Landsat 8 OLI image revealed significant variations in the spectral signatures of the lithological units within the study area. The first three principal components (PC1, PC2, and PC3) captured the majority of the variance (99,54% of the total variance), enabling the differentiation of various serpentine facies types (Table 4).

Table 4 - PCA Eigenvalues and variance (in %) of the Landsat-8 OLI image

PCA bands	Eigenvalues	Variance %
PC1	0.2056	93.58
PC2	0.0071	3.23
PC3	0.006	2.73

Table 5 - MNF Eigenvalues and variance (%) of the Landsat-8 OLI image

MNF bands	Eigenvalues	Variance %
MNF1	0.9733	62.80
MNF2	0.1902	12.27
MNF3	0.1461	9.43

The Ait Ahmane serpentinite massif is primarily composed of Meta-Dunite and Meta-Harzburgite, visually represented by shades of light to dark green on the Landsat-8 OLI image (Fig. 9). These two rock types constitute the main components of the massif, highlighting their extensive distribution throughout the area. By contrast, the gabbros and pyroxenites, which appear in shades ranging from light to dark orange, are present as bands surrounding the serpentinite massif or occur in even more restricted zones within the areas of Jbel Inguijjem and Oumaro.

Minimum Noise Fraction (MNF)

The obtained components allow for a clear distinction of the different lithologies. The first three components, which explain the majority of the variance (Table 5), contain the most relevant geological information. For this reason, the MNF1, MNF2, and MNF3 components were combined into an RGB composite to better visualize and differentiate the lithological boundaries.

The contrasts between the different types of rocks are better defined: the meta-harzburgite appears in light green, while the meta-dunite is distinguished by a yellow hue, reflecting its dominance in the massif (Fig. 10). The areas of gabbros-pyroxenite, represented by shades ranging from light blue to purple, are limited and clearly localized, making them easier to identify. In contrast, the meta-wehrlite does not show a clear contrast, making its delineation more difficult.

Independent Component Analysis (ICA)

The facies map created using Independent Component Analysis (ICA) provides a detailed and distinct visualization of the various lithological units within the Ait Ahmane serpentinite massif. By utilizing spectral bands 1, 2, and 4 from

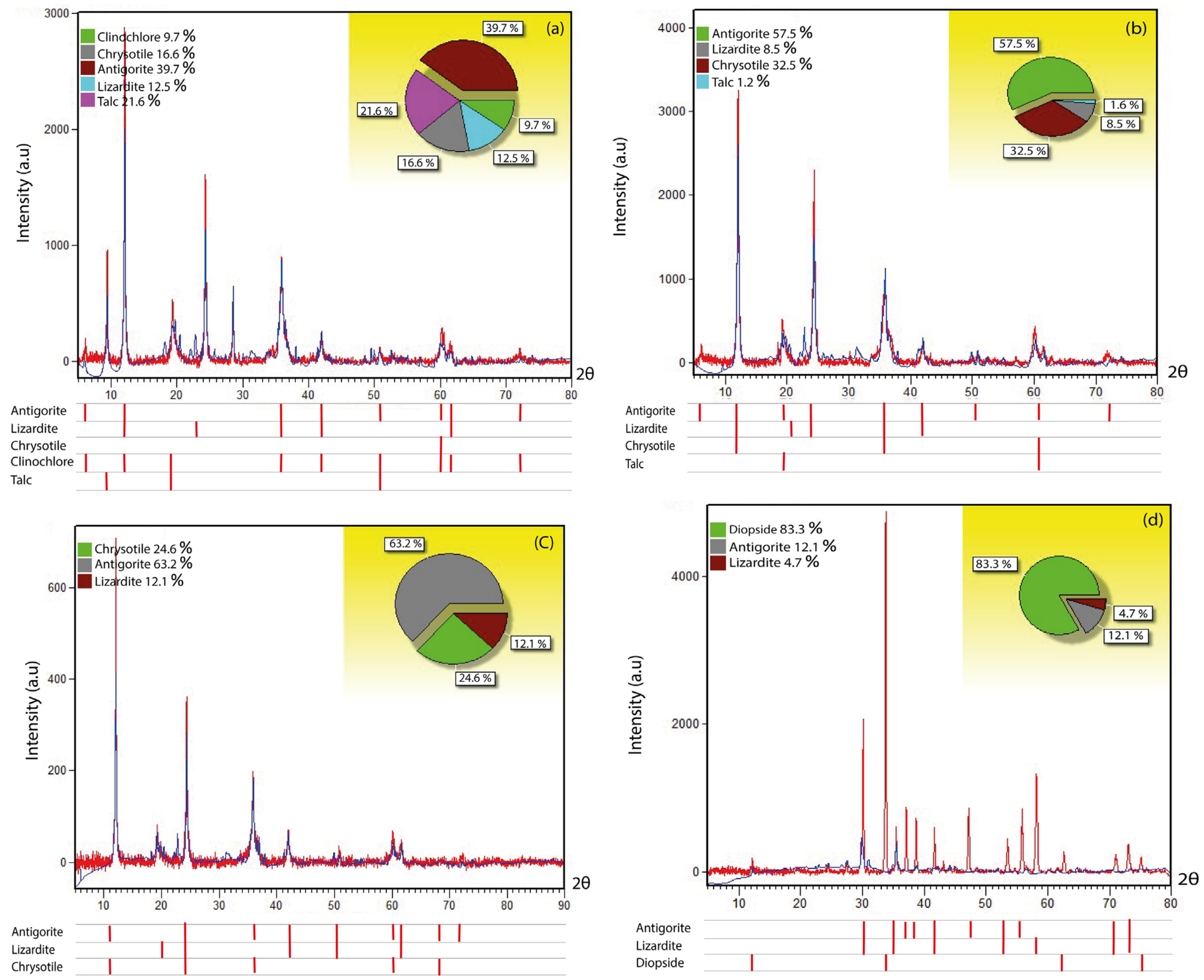

Fig. 7- X-ray diffraction (XRPD) patterns showing the mineralogical assemblage of metamorphosed ultramafic rocks: (a) Meta-dunite (specimen BMAA35), (b) Meta-wehrlite (specimen SA), (c) Meta-harzburgite (specimen BMAA5b), and (d) Meta-pyroxenite (specimen BMI2). The red profile represents the observed experimental data, and the blue profile corresponds to the calculated model. Vertical tick marks indicate the Bragg reflection positions of the identified mineralogical phases. Atg: antigorite; Lz :lizardite; Tlc : talc; Clt : chrysotile ; Clc : clinochlore; En : enstatite; Di : diopside.

the Landsat 8 OLI image, the contrasts between the different facies were enhanced. This combination of bands is particularly effective because band 1 (coastal aerosol) highlights subtle variations in surface composition, while band 2 (blue) enhances the differentiation of mineralogical and textural features. Band 4 (red) contributes to distinguishing between vegetation and bare soil, further improving the contrast between lithological units and facilitating their classification (Yang et al., 2024). The application of ICA allowed for the separation of independent spectral components, thereby improving the discrimination between the various facies present (Tamilarasan et al., 2023) (Fig. 11). Meta-dunites, characterized by their pale yellow to orange hue on lithological classification images, are the most abundant rocks in the massif. Although less common, meta-harzburgites are often found in association with meta-dunites and are distinguished by their light green color. Additionally, the gabbros and meta-pyroxenites, represented by shades ranging from light blue to dark blue, exhibit similar characteristics to those previously mentioned.

Support Vector Machine Classification (SVM)

In this study, the identification of ROIs, used as inputs to classify the three satellite datasets and validate the results with the help of ground control points, was primarily based on detailed field observations with the sampling of 124 samples, and next, using mineralogical characterization. These analyses allowed the definition of five distinct lithological zones. These zones were identified in Landsat-8 OLI imagery, facilitating the precise delineation of the ROIs and the generation of SVM maps with high accuracy.

To further quantify the performance of the SVM classifier and evaluate the relative effectiveness of the different band configurations, a detailed accuracy assessment was carried out using the confusion matrices and standard statistical metrics: overall accuracy (OA), producer’s accuracy (PA), user’s accuracy (UA), and Kappa coefficient). The results, summarized in Table 6, show significant variability in classification performance depending on the spectral transformation applied.

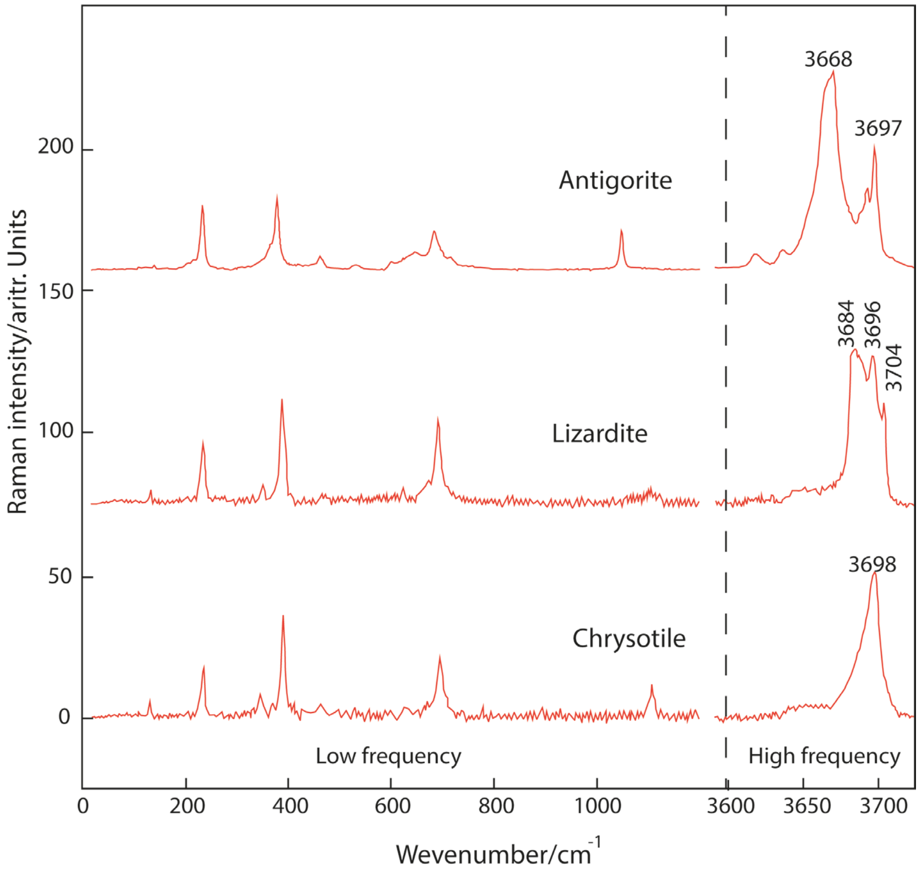

Fig. 8 - Representative Raman spectra of serpentine polymorphs identified in the ultramafic rocks: antigorite, lizardite, and chrysotile. The locations of the analysis points are indicated on the thin section photomicrographs shown in Figure 6.

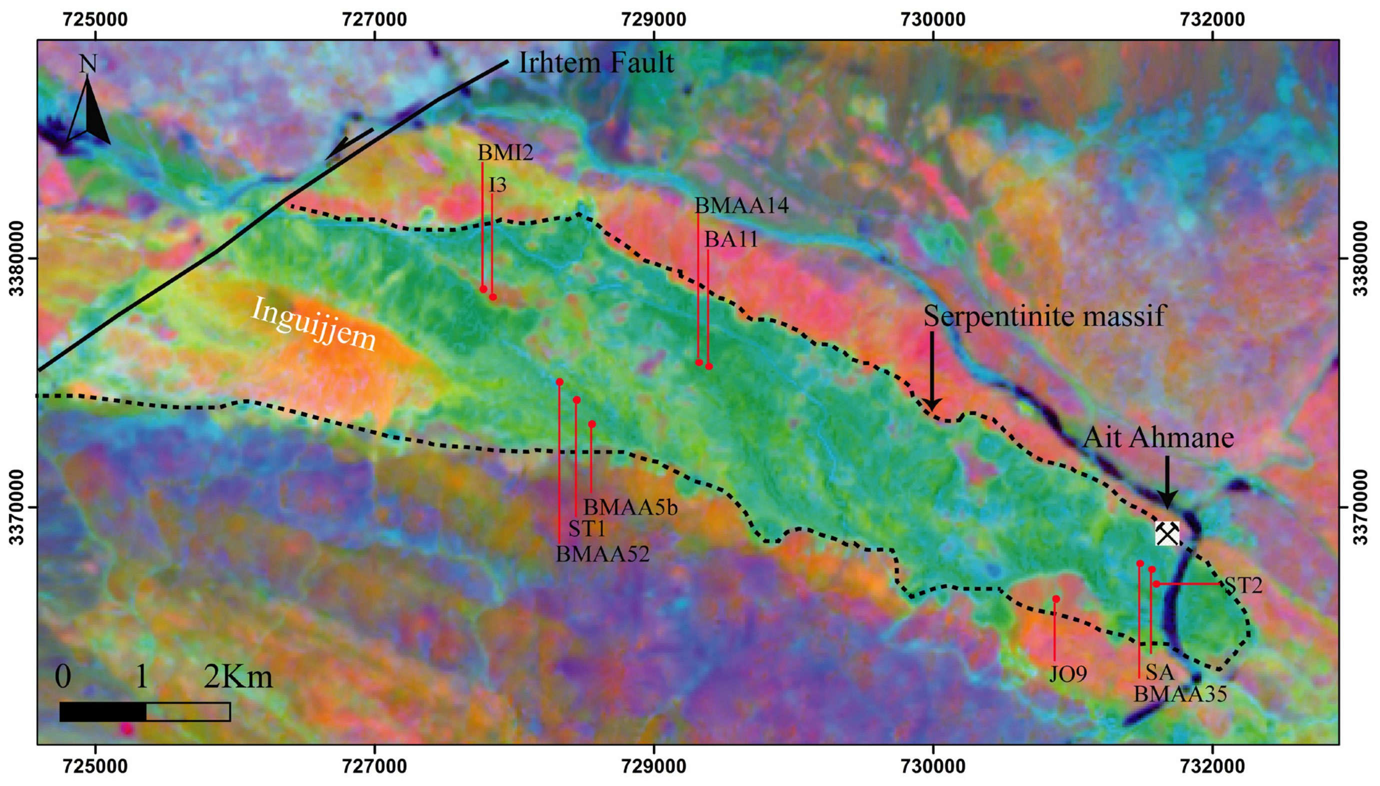

Fig. 9 - Principal Component Analysis (PC1, PC2, and PC3 as RGB) of Landsat-8 OLI image of the Ait Ahmane serpentinite massif.

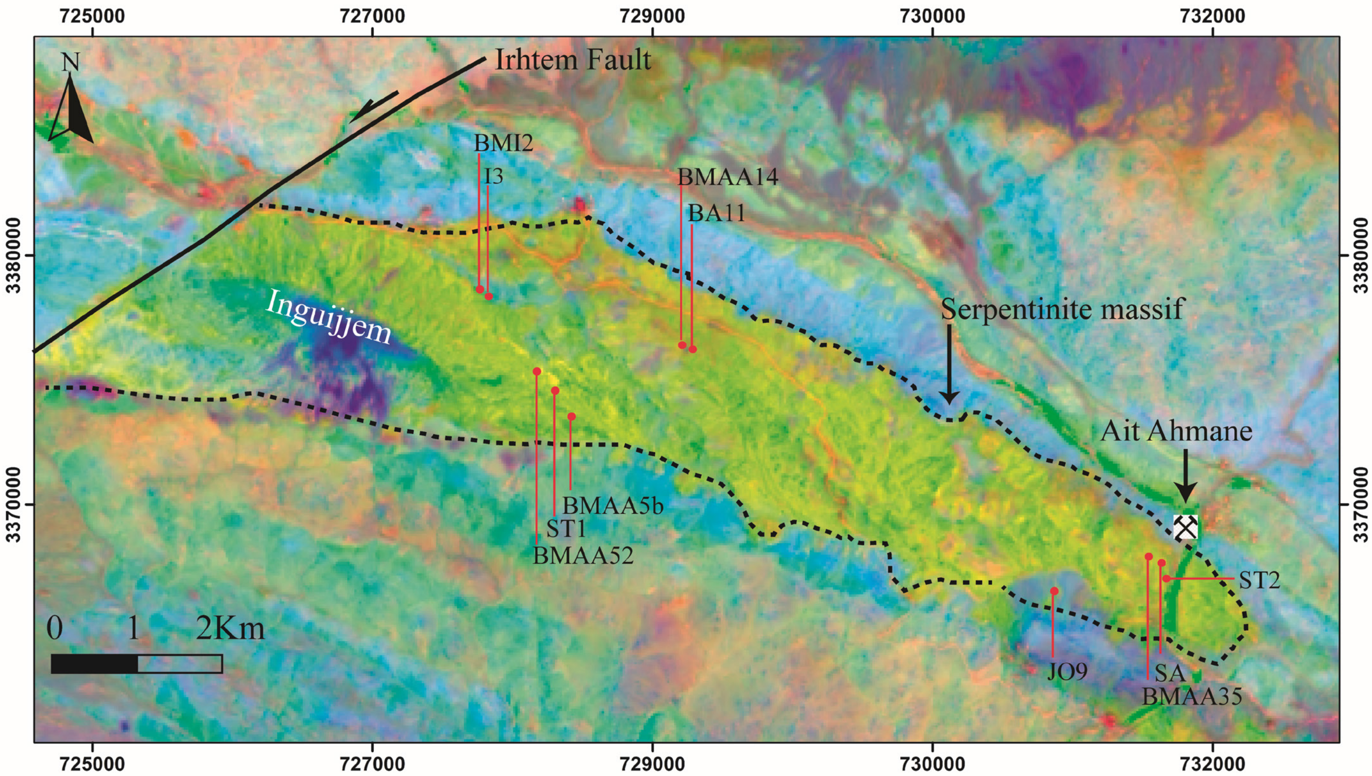

Fig. 10 - Minimum Noise Fraction (MNF) (bands 1, 2, and 3 as RGB) of Landsat 8 OLI image of the Ait Ahmane serpentine massif.

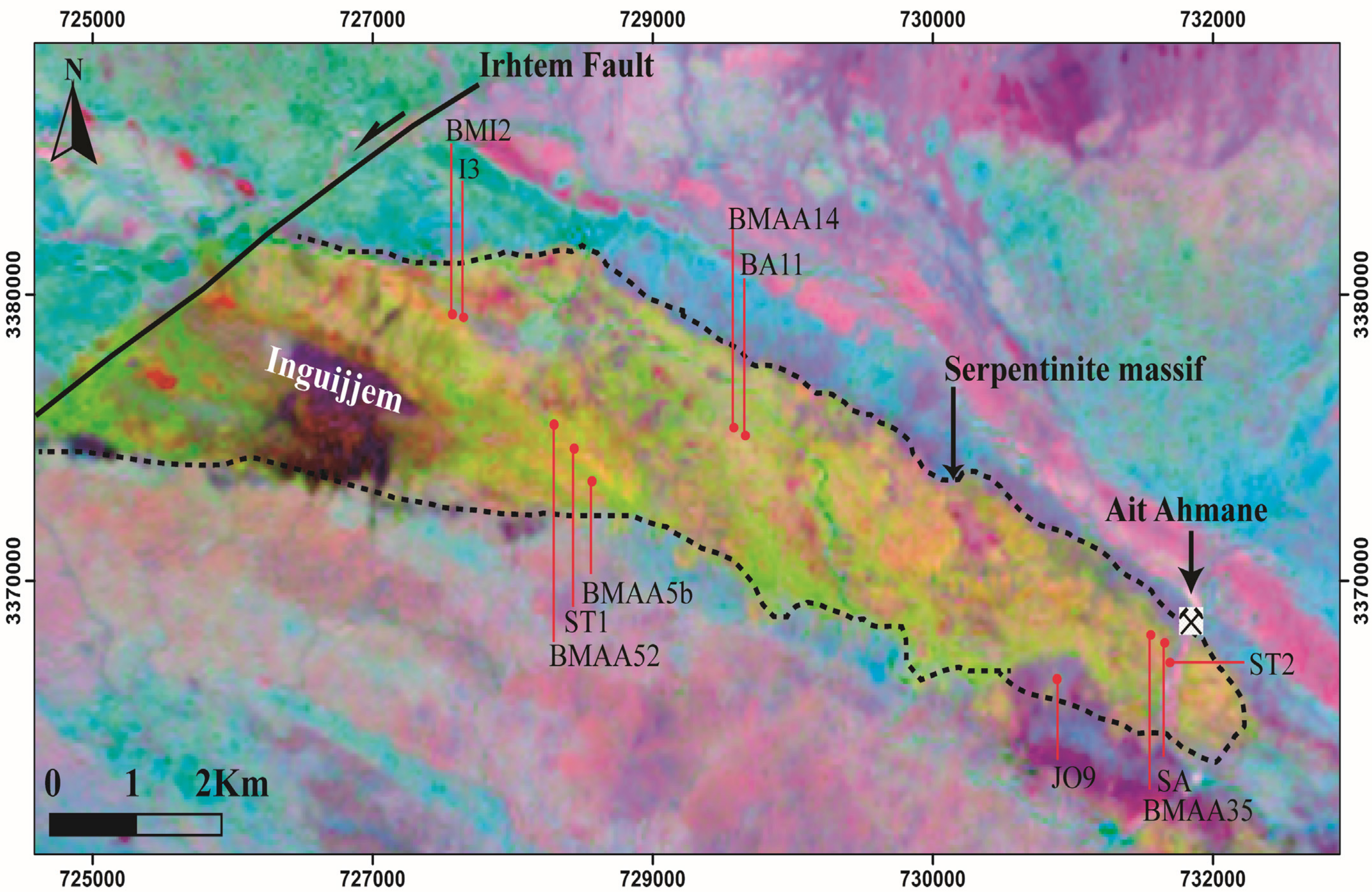

Fig. 11 - Independent Component Analysis (ICA) (bands 1, 2, and 4 as RGB) of Landsat 8 OLI image of the Ait Ahmane serpentine massif.

Table 6 - Confusion Matrix, Overall Accuracy, and Kappa Coefficient for the Landsat-8 Image, Including Results for Pan_sharpening_Oli8, PCA Bands, MNF Bands, and ICA Bands Using the SVM Classification Algorithm

	Class	Cls	Meta-D	Meta-H	Px-Gb	Q-D	Producer's Accuracy (%)	User's Accuracy (%)		
Pan_Sharpening_Oli8	Unclassified	0	0	0	0	0			Overall Accuracy = (119/122) 97.54%	Kappa Coefficient = 0.97
	Cls	14	1	0	0	0	100.00	93.33		
	Meta-D	0	9	0	0	0	75.00	100.00		
	Meta-H	0	2	35	0	0	100.00	94.59		
	Px-Gb	0	0	0	46	0	100.00	100.00		
	Q-D	0	0	0	0	15	100.00	100.00		
	Total	14	12	35	46	15				
PCA Bands	Unclassified	0	0	0	0	0			Overall Accuracy = (113/122) 92.62%	Kappa Coefficient = 0.90
	Cls	14	0	0	0	0	100.00	100.00		
	Meta-D	0	5	2	0	0	41.67	71.43		
	Meta-H	0	7	33	0	0	94.29	82.50		
	Px-Gb	0	0	0	46	0	100.00	100.00		
	Q-D	0	0	0	0	15	100.00	100.00		
	Total	14	12	35	46	15				
MNF Bands	Unclassified	0	0	0	0	0			Overall Accuracy = (112/122) 91.80%	Kappa Coefficient = 0.89
	Cls	14	0	0	0	0	100.00	100.00		
	Meta-D	0	3	1	0	0	25.00	75.00		
	Meta-H	0	9	34	0	0	97.14	79.07		
	Px-Gb	0	0	0	46	0	100.00	100.00		
	Q-D	0	0	0	0	15	100.00	100.00		
	Total	14	12	35	46	15				
ICA Bands	Unclassified	0	0	0	0	0			Overall Accuracy = (107/122) 87.70%	Kappa Coefficient = 0.83
	Cls	12	0	0	0	0	85.71	100.00		
	Meta-D	0	2	2	0	0	16.67	50.00		
	Meta-H	0	8	33	0	0	94.29	80.49		
	Px-Gb	2	1	0	45	0	97.83	93.75		
	Q-D	0	1	0	1	15	100.00	88.24		
	Total	14	12	35	46	15				

The Pan-sharpened Landsat-8 OLI dataset produced the highest classification performance, with an OA of 97.54% and a Kappa coefficient of 0.9665, indicating *near-perfect* agreement with the reference data. All classes except Meta-D achieved a perfect PA and UA (100%), demonstrating excellent separability and minimal spectral confusion. The Meta-D class itself achieved a PA of 75% and a UA of 100%, representing a substantial improvement compared to the other band configurations.

The PCA-derived bands yielded an OA of 92.62% and $\varkappa$ = 0.8989, confirming high performance but with increased misclassification within the Meta-D and Meta-H classes. Specifically, Meta-D showed a PA of 41.67%, reflecting pronounced spectral overlap with Meta-H, which itself achieved a PA of 94.29%. The remaining lithological units (Cls, Px-Gb, Q-D) reached 100% accuracy for both metrics, indicating their strong separability in PCA space.

Similar results were obtained for the MNF transformation (OA = 91.80%, $\varkappa$ = 0.8870). As in the PCA case, the primary sources of error were concentrated in the Meta-D class, which exhibited the lowest PA across all transformations (25%). Meta-H achieved very high PA (97.14%), confirming the systematic confusion between these two metasomatic units.

Conversely, the ICA bands showed the lowest performance, with OA = 87.70% and $\varkappa$ = 0.8301. Misclassification increased across multiple classes, particularly for Cls

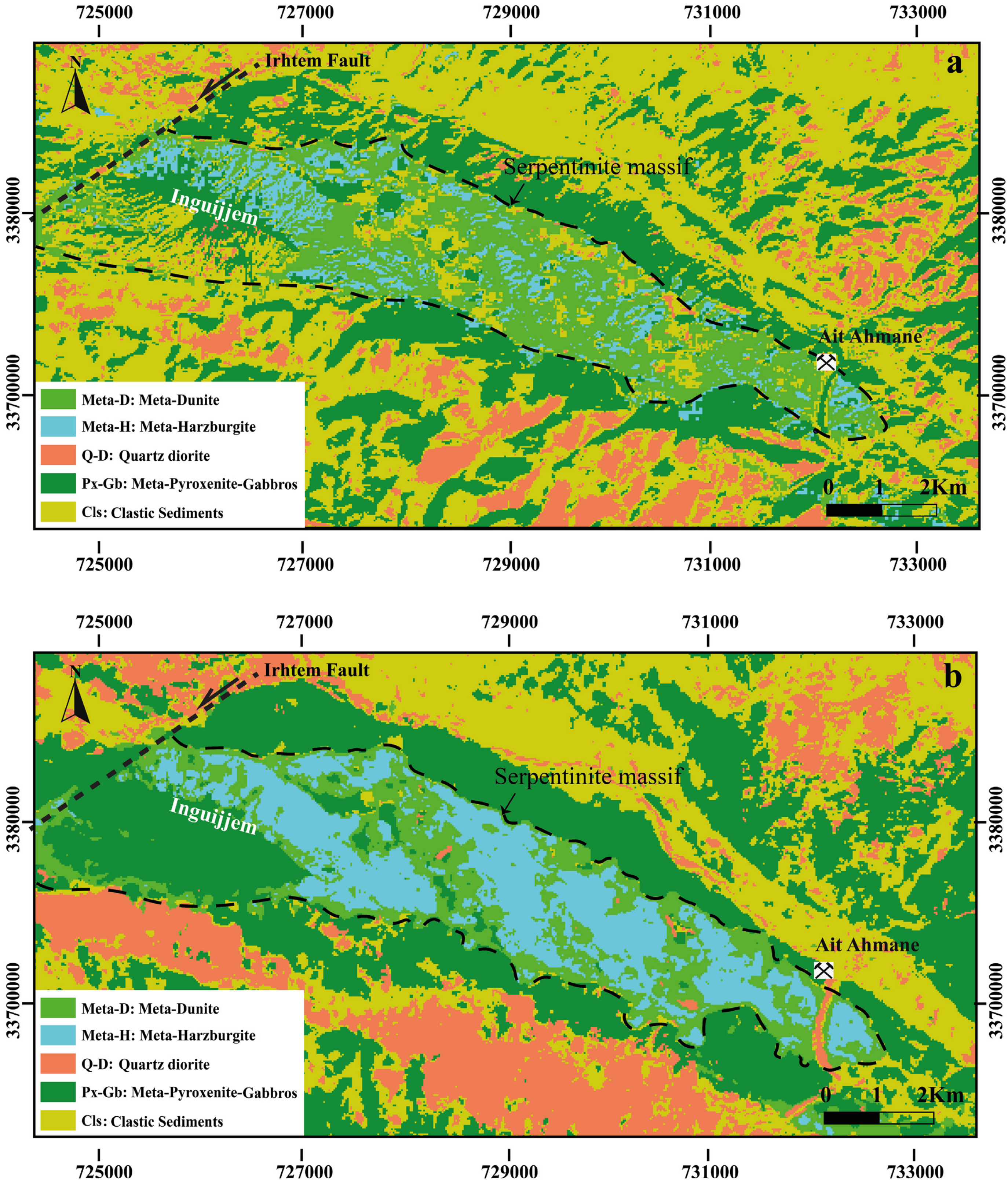

Fig. 12 - SVM map of the Landsat-8 OLI image in the Inguijjem Ait Ahmane massif study area. a) Pan_sharpening_Oli8, b) PCA bands, c) MNF bands, and d) ICA bands.

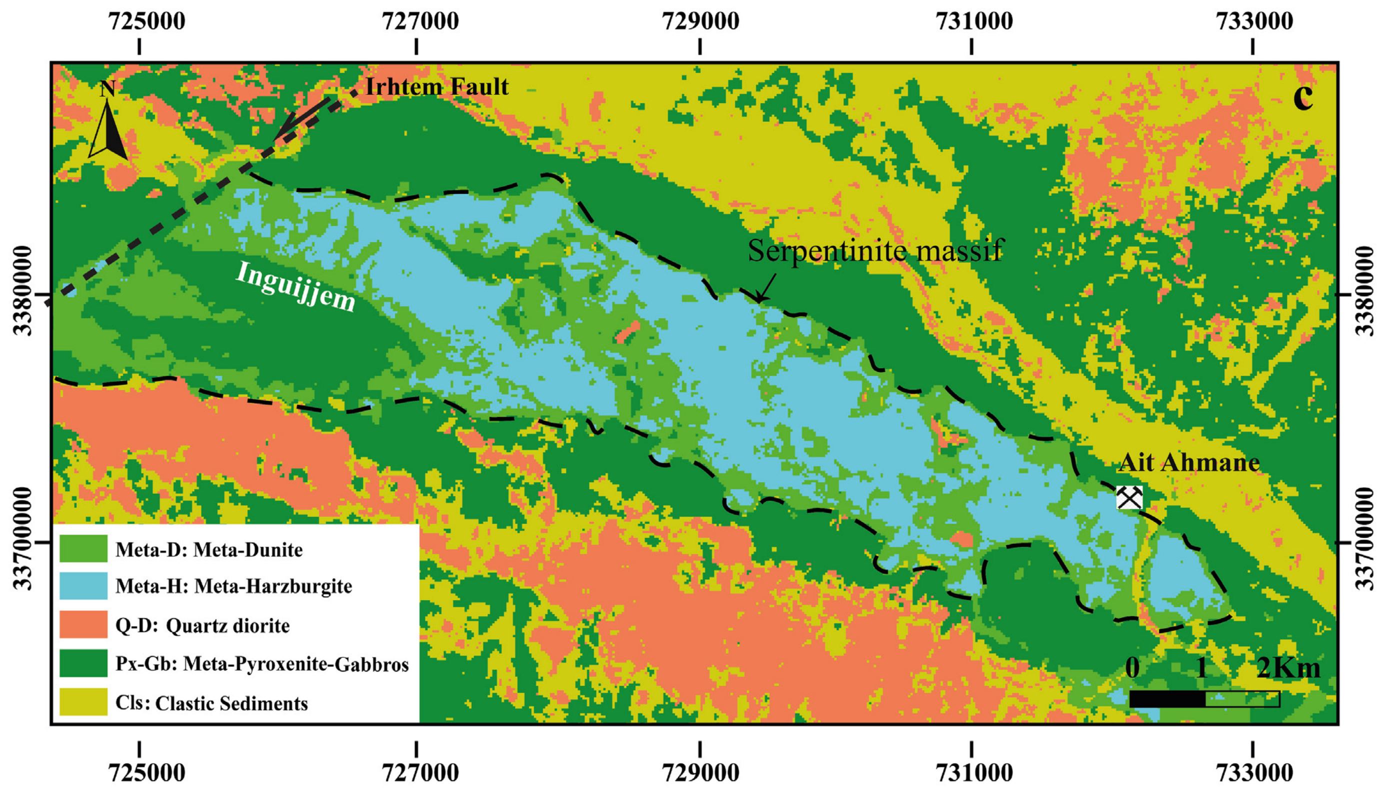

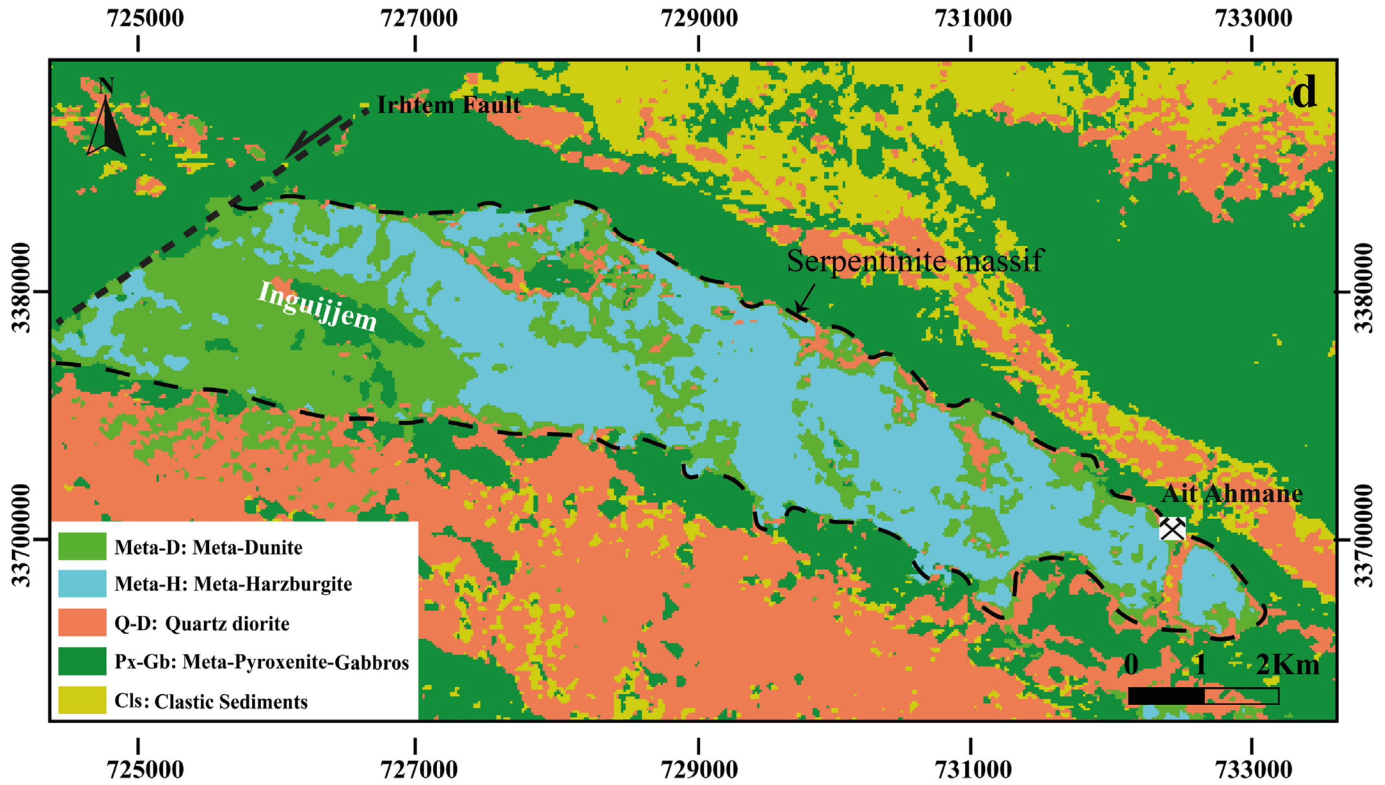

Fig. 12 *(continues)*

(producer accuracy reduced to 85.71%) and Meta-D (PA 16.67%, UA 50%), highlighting the limited discriminative capability of independent components for this dataset.

Quantitative analysis of the SVM classification map allows for a precise assessment of the spatial distribution of the identified lithologies. The total classified area covers approximately 447.67 km^2. The study area is widely dominated by the Cls unit (likely sedimentary cover or quaternary deposits) and the Px-Gb facies (Gabbro-Pyroxenites), which cover 209.98 km^2 (46.91%) and 175.20 km^2 (39.14%) respectively. The Q-D (Quartz-Diorite) unit occupies an intermediate position, extending over 44.00 km^2 (9.83%).

In contrast, the ultramafic sequences appear as subordinate facies within the massif. The Meta-Dunites account for 9.41 km^2 (2.10%), while the Meta-Harzburgites occupy a nearly equivalent area of 9.08 km^2 (2.03%). This statistical distribution highlights that, although mineralogically distinct and economically significant, the serpentinized ultramafic bodies are spatially restricted compared to the dominant mafic and sedimentary formations in this sector of the ophiolite.

Overall, the comparative analysis demonstrates that the Pan-sharpened OLI bands significantly outperform all other spectral transformations, with improvements of +4.92% (vs. PCA), +5.74% (vs. MNF), and +9.84% (vs. ICA) in OA, and corresponding increases in Kappa of +0.0676, +0.0795, and +0.1364, respectively. These results confirm that spatial enhancement of the multispectral data strongly benefits SVM performance, particularly for lithologically complex classes such as Meta-D, which show reduced confusion when using higher spatial resolution input.

Figure 12 presents the results and the highly accurate, reliable classification map of the study area using the Landsat-8 OLI image.

DISCUSSION

Contrary to previous descriptions that simplified the Inguijjem-Ait Ahmane massif as a homogeneous serpentinized body (Leblanc, 1981; Admou et al., 2013), our mineralogical and petrographic data reveal a complex lithological history. Indeed, the XRD and Raman investigation, which have been carried out on representative lithotypes confirm that the heterogeneity observed is not random since it stems from distinct protoliths (dunite vs. harzburgite vs. pyroxenite) that underwent various degrees of serpentinization.

The identification of specific serpentine polymorphs offers critical insights into the thermodynamic evolution of the complex. We identified the coexistence of lizardite/chrysotile and antigorite. While lizardite and chrysotile typically form during low-temperature ocean-floor hydration (<300°C) or retrograde metamorphic events, the presence of antigorite indicates a transition to higher-grade metamorphic conditions. This suggests that the massif did not simply undergo static alteration but experienced a polyphase evolution, likely involving an initial oceanic serpentinization followed by another metamorphic event or tectonic emplacement that favored the stability of antigorite.

The WNW-ESE orientation of the facies bands suggests a strong structural control over these metamorphic processes. The transformation of primary silicates into secondary phases (e.g., clinochlore, talc, carbonates) implies significant fluid circulation channeled by these tectonic structures. Consequently, the «complex geological history» of the region can be interpreted as a continuum from magmatic segregation (e.g. forming the various protoliths of pyroxenite) to hydrothermal alteration and subsequent tectonic deformation, leading to the heterogeneous distinct mineralogical assemblages we observe today.

The mineralogical diversity described above provides the physical basis for the spectral heterogeneity detected by our remote sensing approach. Our results demonstrate that the SVM algorithm, particularly when applied to Pan-Sharpened Landsat 8 data, successfully discriminates these lithological variations with a high accuracy (97.54%).

Comparison with similar studies highlights the robustness of this method. Similar approaches using SVM and band ratios have been successfully applied to ophiolitic complexes in arid environments, such as the Eastern Desert of Egypt (Amer et al., 2010; Ghoneim et al., 2024 ; Shereif et al., 2024), the Zagros belt in Iran (Khaneghah and Arfania, 2017), and ophiolites in Turkey (Ekici, 2023). However, our study shows that integrating Pan-Sharpening significantly refines the classification of ultramafic sub-units (Meta-dunite vs. Meta-harzburgite) compared to using standard spectral bands alone, as often done in earlier works.

The cross-validation between laboratory data (XRD/Raman) and satellite imagery confirms that the spectral heterogeneity of the Ait Ahmane-Inguijjem massif is a direct proxy for its lithological and metamorphic diversity. This validates the use of advanced machine learning techniques (SVM) as a reliable tool for updating geological maps of complex metamorphic terrains where traditional field mapping is challenged by accessibility or visual homogeneity.

Ultimately, this integrated approach provides a cost-effective framework for guiding mineral exploration in the Anti-Atlas. By accurately delineating ultramafic subunits – particularly the distinction between meta-dunites and meta-harzburgites–this method allows for the precise targeting of host rocks for economic mineralization. This spatial refinement is particularly relevant in light of recent findings by Wafik et al., (2024, 2025b), who emphasized the critical control of lithology and structural setting on the genesis of mineralization in the Bou Azzer district.

Furthermore, beyond its economic implications, this study contributes to deciphering the fundamental geology of the region. The detailed lithological heterogeneity unveiled here serves as a cornerstone for our ongoing research. We are currently using these high-resolution spectral and mineralogical constraints to construct a comprehensive geodynamic model of the emplacement of the Ait Ahmane-Inguijjem ophiolitic complex, aiming to reconstruct the polyphase tectonic history of this segment of the Pan-African belt.

CONCLUSIONS

The multi-analytical approach employed in this study on the Inguijjem-Aït Ahmane serpentinite massif allowed to highlight the occurring lithological variations; indeed, interpretations obtained by using advanced remote sensing techniques were validated through laboratory analyses, particularly X-ray Powder Diffraction (XRPD) and Raman spectroscopy. The integration of satellite data with mineralogical ground-truthing successfully confirmed the marked heterogeneity of the massif, challenging previous assumptions of a homogeneous composition. Our results demonstrate that the spectral variations mapped by the SVM algorithm – specifically when applied to Pan-Sharpened Landsat-8 data correspond to intrinsic lithological differences (e.g. meta-dunites vs. meta-harzburgites) rather than random secondary alteration. This distinction is crucial as it reveals a complex geological history involving polyphase serpentinization and tectonic deformation.

Beyond these fundamental geological insights, this work has also significant practical applications for the mining industry. The ability to remotely discriminate between specific ultramafic sub-units provides a cost-effective and non-invasive tool for mineral exploration, particularly for targeting cobalt, nickel, and chromite mineralizations, known to be structurally and lithologically controlled in the Bou Azzer district. By narrowing down target zones, this approach optimizes field campaigns and surveys in inaccessible areas. Future research will focus on integrating these high-resolution lithological constraints into a broader 3D geodynamic model, aiming to reconstruct the emplacement mechanisms of the ophiolitic complex within the Pan-African belt.

ACKNOWLEDGEMENTS

We thank the reviewers for their constructive comments and suggestions, which improved the original manuscript. We also gratefully acknowledge the editorial handling of this paper.

ONLINE SUPPLEMENTARY MATERIAL

Supplementary data to this article are available online at https://doi.org/10.4454/ofioliti.v51i2.591

REFERENCES

Adiri Z., El Harti A., Jellouli A., Maacha L., Azmi M., Zouhair M. and El Bachaoui E.M., 2020. Mineralogical mapping using Landsat-8 OLI, Terra ASTER and Sentinel-2A multispectral data in Sidi Flah-Bouskour inlier, Moroccan Anti-Atlas. *J. Spat. Sci.*, 65(1), 147-171. https://doi.org/10.1080/14498596.2018.1490213

Admou H., Razin P., Egal E., Youbi N., Soulaimani A., et al.., 2013. Notice explicative de la Carte géologiques du Maroc (1/50 000), feuille Aït Ahmane. Notes et Mémoires du service Géologique du Maroc, 2013, 533 bis. ⟨halsde-00950547⟩

Amer R., Kusky T. and Ghulam A., 2010. Lithological mapping in the Central Eastern Desert of Egypt using ASTER data. J. Afr. Earth Sci., 56(2-3), 75-82. https://doi.org/10.1016/j.jafrearsci.2009.06.004

Amer R., Kusky T. and El Mezayen A., 2012. Remote sensing detection of gold related alteration zones in Um Rus area, Central Eastern Desert of Egypt. Adv. Space Res., 49(1), 121–134. https://doi.org/10.1016/j.asr.2011.09.024

Bentahar I. and Raji M., 2021. Comparison of Landsat OLI, ASTER, and Sentinel 2A data in lithological mapping: A Case study of Rich area (Central High Atlas, Morocco). Adv. Space Res., 67(3), 945-963. https://doi.org/10.1016/j.asr.2020.10.038

Black R., Ba H., Ball E., Bertrand J.M., Boullier A.M., Caby R., Davison I., Fabre J., Leblanc M. and Wright L.I., 1979. Outline of the Pan-African geology of Adrar des Iforas (Republic of Mali). Geol. Rundsch., 68(2), 543–564. https://doi.org/10.1007/BF01820806

Black R., Latouche L., Liégeois J.P., Caby R. and Bertrand J.M., 1994. Pan-African displaced terranes in the Tuareg shield (central Sahara). Geology, 22(7), 641-644. https://doi.org/10.1130/0091-7613(1994)022<0641:PADTIT>2.3.CO;2

Blein O., Baudin T., Soulaimani A., Cocherie A., Chèvremont P., Admou H., Ouanaimi H., Hafid A., Razin P., Bouabdelli M. and Roger J., 2014. New geochemical, geochronological and structural constraints on the Ediacaran evolution of the south Sirwa, Agadir-Melloul and Iguerda inliers, Anti-Atlas, Morocco. J. Afr. Earth Sci., 98, 47-71. https://doi.org/10.1016/j.jafrearsci.2014.06.019

Bodinier J.L., Dupuy C. and Dostal J., 1984. Geochemistry of Precambrian ophiolites from Bou Azzer, Morocco. Contrib. Mineral. Petrol., 87(1), 43-50. https://doi.org/10.1007/BF00371401

Bonnemains D., Reynar B., Vandemeulebrouck J., Ricard Y. and French Network of Seismic Survey E., 2016. Seismic noise correlations across the Provence region, southeastern France: Investigating the lithospheric structure and the crust-mantle boundary. J. Geophys. Res. Solid Earth, 121(2), 964-978. https://doi.org/10.1002/2015JB012507

Congalton R. G., and Green K. 2019. Assessing the accuracy of remotely sensed data. Principles and Practices. Third Edition (3rd ed.), CRC press. Taylor and Francis, Boca Raton, 346 pp. https://doi.org/10.1201/9780429052729

Ekici T., 2023. Lithological mapping of ophiolitic rocks from southern part of the Sivas Basin (Turkey) using ASTER imagery. Turk. J. Earth Sci., 32(2), 200-213. https://doi.org/10.55730/1300-0985.1842

El Hadi H., Simancas J.F., Martínez-Poyatos D., Azor A., Tahiri A., Montero P., Fanning C.M., Bea F. and González-Lodeiro F., 2010. Structural and geochronological constraints on the evolution of the Bou Azzer Neoproterozoic ophiolite (Anti-Atlas, Morocco). Precambrian Res., 182(1-2), 1-14. https://doi.org/10.1016/j.precamres.2010.06.011

Ennih N. and Liégeois J.P., 2001. The Moroccan Anti-Atlas: The West African craton passive margin with limited Pan-African activity. Implications for the northern limit of the craton. Precambrian Res., 112(3-4), 289-302. https://doi.org/10.1016/S0301-9268(01)00195-4

Ennih N. and Liégeois J.P., 2008. The boundaries of the West African craton, with special reference to the basement of the Moroccan metacratonic Anti-Atlas belt. Geol. Soc. Lond. Spec. Publ., 297(1), 1-17. https://doi.org/10.1144/SP297.1

Gasquet D., Ennih N., Liégeois J.P., Soulaimani A. and Michard A., 2008. The Pan-African Belt. In: Ennih N. and Liégeois J.P. (Eds.), The Boundaries of the West African Craton, Geological Society, London, Special Publications, 297, 33–64. https://doi.org/10.1144/SP297.2

Ge W., Cheng Q., Jing L., Armenakis C. and Ding H., 2018. Lithological discrimination using ASTER and Sentinel-2A in the Shibanjing ophiolite complex of Beishan orogenic in Inner Mongolia, China. Adv. Space Res., 62(7), 1702-1716. https://doi.org/10.1016/j.asr.2018.06.036

Ghoneim S.M., Hamimi Z., Abdelrahman K., Khalifa M.A., Shabban M. and Abdelmaksoud A.S., 2024. Machine learning and remote sensing-based lithological mapping of the Duwi Shear-Belt area, Central Eastern Desert, Egypt. Sci. Rep., 14, 17010. https://doi.org/10.1038/s41598-024-67851-x

Hefferan K.P., Admou H., Karson J.A. and Saquaque A., 2000. Anti-Atlas (Morocco) role in Neoproterozoic Western Gondwana reconstruction. Precambrian Res., 103(1-2), 89-96. https://doi.org/10.1016/S0301-9268(00)00078-4

Hefferan K., Soulaimani A., Samson S.D., Admou H., Inglis J., Saquaque A., Chaib L. and Heywood N., 2014. A reconsideration of Pan African orogenic cycle in the Anti-Atlas Mountains, Morocco. J. Afr. Earth Sci., 98, 34-46. https://doi.org/10.1016/j.jafrearsci.2014.03.007

Inglis J.D., D'Lemos R.S., Samson S.D. and Admou H., 2005. Geochronological constraints on Late Precambrian intrusion, metamorphism, and tectonism in the Anti-Atlas Mountains. J. Geol., 113(4), 439-450. https://doi.org/10.1086/430242

Khaneghah A.R.N. and Arfania R., 2017. Lithological analysis of Nain Ophiolitic zone using ASTER data. Open J. Geol., 7(8), 1200-1214. https://doi.org/10.4236/ojg.2017.78080

Khurram S., Khakil Rao Z., Beiranvand Pour A., Riaz K., Fatima A. and Ahmed A., 2025. ASTER and Hyperion satellite remote sensing data for lithological mapping and mineral exploration in ophiolite zones: a case study from Lasbela, Baluchistan, Pakistan. Mining, 5, 53. https://doi.org/10.3390/mining5030053

Klein F., Bach W. and McCollom T.M., 2013. Compositional controls on hydrogen generation during serpentinization of ultramafic rocks. Lithos, 178, 55-69. https://doi.org/10.1016/j.lithos.2013.03.008

Leblanc M., 1975. Ophiolites précambriennes et gites arséniés de cobalt (Bou-Azzer, Maroc). Master's Thesis, Université de Paris VI, Paris. https://www.scirp.org/reference/referencespapers?referenceid=3608306

Leblanc M., 1981. The Late Proterozoic Ophiolites of Bou Azzer (Morocco): Evidence for Pan-African Plate Tectonics. Dev. Precambrian Geol., 4, 435-451. https://doi.org/10.1016/S0166-2635(08)70022-7

Marzouki A. and Dridri A., 2023. Lithological discrimination and structural lineaments extraction using Landsat 8 and ASTER data: a case study of Tiwit (Anti-Atlas, Morocco). Environ. Earth Sci., 82, 125. https://doi.org/10.1007/s12665-023-10831-4

Naidoo D.D., Bloomer S.H., Saquaque A. and Hefferan K., 1991. Geochemistry and significance of metavolcanic rocks from the Bou Azzer-El Graara ophiolite (Morocco). Precambrian Res., 53(1-2), 79-97. https://doi.org/10.1016/0301-9268(91)90006-V

Saquaque A., Admou H., Cisse A., Benyoucef A.H. and Reuber I., 1989. Les intrusions calco-alcalines de la boutonnière de Bou Azzer-El Graara (Anti-Atlas, Maroc): marqueurs de la déformation panafricaine majeure dans un contexte de collision d'arc. C.R. Acad. Sci. Paris, 308(14), 1279-1283.

Shereif A.S., Shebl A., Mahmoud A.S. and Csámer Á., 2024. Enhanced lithological mapping in El-Missikat and El-Erediya areas, central Eastern desert, Egypt, leveraging remote sensing techniques and machine learning algorithms. IEEE Trans. Geosci. Remote Sens., 62, 1-27. https://doi.org/10.1109/TGRS.2024.3351283

Soulaimani A., Ouanaimi H. and Saddiqi O., 2018. The Anti-Atlas Pan-African Belt (Morocco): Overview and pending questions. C.R. Geosci., 350(6), 279-288. https://doi.org/10.1016/j.crte.2018.07.002

Tamilarasan K., Anbazhagan S. and Ranjithkumar S., 2023. Rock type discrimination using Landsat-8 OLI satellite data in mafic-ultramafic terrain. Geol. Geophys. Environ., 49(3), 281–298. https://doi.org/10.7494/geol.2023.49.3.281

Tzvetanova Y., Petrov O., Kerestedjian T., Tarassov M., 2020. Quantitative Phase Analysis of Skarn Rocks by the Rietveld Method Using X-ray Powder Diffraction Data. *Minerals*, 10(10):894. https://doi.org/10.3390/min10100894

Thomas R.J., Chevallier L.P., Gresse P.G., Harmer R.E., Eglington B.M., Armstrong R.A., de Beer C.H., Martini J.E.J., de Kock G.S., Macey P.H. and Ingram B.A., 2002. Precambrian evolution of the Sirwa Window, Anti-Atlas Orogen, Morocco. Precambrian Res., 118(1-2), 1-57. https://doi.org/10.1016/S0301-9268(02)00075-X

Vapnik V.N., 1999. The Nature of Statistical Learning Theory. 2nd ed., Springer, New York, 314 pp. https://doi.org/10.1007/978-1-4757-3264-1

Wafik A., 2001. Étude Géochimique et Métallogénique d'un Système Hydrothermal Océanique Fossile : Exemple des Minéralisations Cuprifères dans les Ophiolites Protérozoïques de l'Anti-Atlas Central (Maroc). Thèse de Doctorat, Université Cadi Ayyad, Marrakech, 314 pp.

Wafik A., Admou H., Saquaque A., El Boukhari A. and Juteau T., 2001a. Les minéralisations sulfurées à Cu-Fe et les altérations associées dans les ophiolites protérozoïques de Bou Azzer et de Khzama (Anti-Atlas, Maroc). Ofioliti, 26(1), 47-62. https://doi.org/10.4454/ofioliti.v26i1.130

Wafik A., Bhilisse M., Admou H., Maacha L., Elghorfi M. and Constantin M., 2015. The Podiform Chromite and Platinum Group Elements in the Neoproterozoic Ophiolite Bou Azzer (Inlier Bou Azzer - El Graara, central Anti-Atlas). Eur. Sci. J., 11(36), 121-140. https://doi.org/10.19044/esj.2015.v11n36p%25p

Wafik A., Saquaque A. and El Boukhari A., 2001b. Les chromitites podiformes et les minéraux de Fe-Cu-Ni-Co associés à l'ophiolite de Bou Azzer-el Graara (Anti-Atlas central, Maroc). Ofioliti, 26(2b), 467-478. https://doi.org/10.4454/ofioliti.v26i2b.168

Wafik A., Visalli R., Punturo R., Conte M.A., Guglietta D., Ben Massoude M., El Aouad N., Nzaou Mabika N. and Cirrincione R., 2025a. Neoproterozoic serpentinites from the Bou Azzer ophiolite, Central Anti-Atlas (Morocco): geodynamic evolution and mantle processes beneath the West African Craton boundaries. Ital. J. Geosci., 144(1), 48-69. https://doi.org/10.3301/IJG.2024.03

Wafik, A., Ben massoude, M., Karfal, A., Bajddi, A., Maacha, L. 2025b. A Preliminary Study on Hidden Ni Mineralization and Associated Gold in the Inguijem-Ait Ahmane Serpentinite, Bou Azzer Ophiolite, Morocco: Geodynamic Implications. In: Çiner, A., et al. Recent Research on Sedimentology, Stratigraphy, Paleontology, Tectonics, Geochemistry, Volcanology and Petroleum Geology. MedGU 2023. Advances in Science, Technology and Innovation. Springer, Cham. https://doi.org/10.1007/978-3-031-87558-8_3

Wafik A., Zoheir B., Benchekroun F., Benaouda R., Ben Massoude M., Atif Y., Beiranvand Pour A., Niroomand S., El Arbaoui A., Karfal A. and Maacha L., 2024. Multistage Gold-Polymetallic Mineralization in the Bou Azzer District, Anti-Atlas, Morocco: Insights from Ore Microscopic, Geochemical, and Fluid Inclusion Studies. Geofluids, 2024(1), 5579902. https://doi.org/10.1155/2024/5579902

Walsh G.J., Benziane F., Aleinikoff J.N., Harrison R.W., Yazidi A., Burton W.C., Quick J.E. and Saadane A., 2012. Neoproterozoic tectonic evolution of the Jebel Saghro and Bou Azzer - El Graara inliers, eastern and central Anti-Atlas, Morocco. *Precambrian Res*., 216-219, 23-62. https://doi.org/10.1016/j.precamres.2012.06.010

Yang X., 2011. Parameterizing support vector machines for land cover classification. Photogramm. Eng. Remote Sens., 77(1), 27-38. https://doi.org/10.14358/PERS.77.1.27

Yang C., Jia H., Dong L., Zhao H. and Zhao M., 2024. Selection of Landsat-8 OLI optimal band combinations for mapping alteration zones. Remote Sens., 16(2), 392. https://doi.org/10.3390/rs16020392.

Zhang T., Yi G., Li H., Wang Z., Tan J., Zhong K., Li Y., Wan Q. and Bi X., 2016. Integrating Data of ASTER and Landsat-8 OLI (AO) for Hydrothermal Alteration Mineral Mapping in Duolong Porphyry Cu-Au Deposit, Tibetan Plateau, China. Remote Sens., 8(11), 890. https://doi.org/10.3390/rs8110890

Received, October 2, 2025
Accepted, June 9, 2026